LA-UR-17-24451
Approved for public release; distribution is unlimited.

Title: Hydrated Ordinary Portland Cement as a Carbonic Cement: The Mechanisms, Dynamics, and Implications of Self-Sealing and CO2 Resistance in Wellbore Cements

Author(s): Guthrie, George Drake Jr.
Pawar, Rajesh J.
Carey, James William
Karra, Satish
Harp, Dylan Robert
Viswanathan, Hari S.

Intended for: Report

Issued: 2017-08-15 (rev.2)

Hydrated Portland Cement as a Carbonic Cement:

The Mechanisms, Dynamics, and Implications of Self-Sealing and CO_2 Resistance in Wellbore Cements

George D. Guthrie, Jr., Rajesh Pawar, Bill Carey, Satish Karra, Dylan Harp, Hari Viswanathan

Earth and Environmental Sciences Division
Los Alamos National Laboratory
Los Alamos, NM 87545

LA-UR-17-24451

31 July 2017, R1

Executive Summary

This report analyzes the dynamics and mechanisms of the interactions of carbonated brine with hydrated Portland cement. The analysis is based on a recent set of comprehensive reactive-transport simulations, and it relies heavily on the synthesis of the body of work on wellbore integrity that we have conducted for the Carbon Storage Program over the past decade, including:

- First field core of cement from a CO_2+brine environment, demonstrating self-sealing (Carey et al., 2007); multiple subsequent field cores including in partnership with the CO_2 Capture Project (Crow et al., 2009; Crow et al., 2010)
- First thermodynamic model for cement+brine+CO_2 interactions that addressed C–S–H compositional variation (Carey and Lichtner, 2007, 2011)
- First comprehensive kinetic model for acid–base interactions in the cement system (Guthrie and Carey, 2015)
- Experimental static and flow-through models demonstrating self-sealing in the brine+CO_2+cement system, including in the presence of caprock (Wigand et al., 2009; Newell & Carey, 2012)
- Experimental assessment of corrosion processes involving cement and casing (Carey et al., 2010)
- Measurement and development of permeabilities for wellbore cements and effective permeabilities for wellbores (Carey et al., 2007; 2010)
- Development of a fully coupled physics-based model to simulate flow from a reservoir through a partially cemented well, and an associated reduced-order model (ROM) for rapid emulation of the full-physics simulation of fluid flow along a partially cemented wellbore (Jordan et al., 2015; Harp et al., 2014, 2016)
- Development (and continued evolution) of the first system model for assessing wellbore leakage in a storage system (Viswanathan et al., 2008; Pawar et al., 2014, 2016)

These earlier studies demonstrated wellbore self-sealing can occur. In addition, this work and the concurrent work in the broader community (as part of the Carbon Storage Program and other international efforts) developed tools and the science base needed to simulate the chemical and mineralogical evolution of wellbore integrity and to simulate the leakage behavior of a wellbore in a storage environment.

Despite the large body of work on wellbore integrity across the community, it remains a somewhat open-issue whether a wellbore completed with Portland based cement will always maintain integrity over time in the presence of carbonated brine. This ambiguity ties to the complexity of the system, which embodies a large chemical and mineralogical diversity, a wide range in physical conditions and flow regimes, significant limitations on observing the dynamics directly, and uncertainty in the fundamental parameters needed to simulate all aspects of the dynamics exactly.

In this synthesis report, we clarify some of this ambiguity while developing a basis for answering two questions facing CO_2 storage operations: First, what is a sufficient length of cement along the wellbore to maintain integrity over the design life of a project? Second, what makes a cement "compatible" with a carbonated brine? These questions are central to Class VI permitting considerations. We approach this through a synthesis of the body of knowledge developed during our earlier work and by others in the community over the last decade. We combine this synthesis with the analysis of an extensive set

of simulations that probe the diverse range of conditions, properties, and uncertainties alluded to above.

Specifically, we conducted a set of reactive-transport calculations to elucidate the dynamics of the interactions. Although several recent studies have presented reactive-transport models for this system, we add three important elements in our study to address the factors above:

1) *We focus on constant flow simulations*, avoiding the uncertainties inherent in the coupled processes that occur as the hydraulic properties of the flowpath evolve. Although this approach precludes our ability to simulate exact dynamics for a specific scenario, it nevertheless captures the physics and chemistry of the system accurately, and the results provide insights that have been previously obscured in the more complicated model systems.
2) *We explicitly assess the uncertainty and variability in the thermodynamic and kinetic models for the system.* This allows us to evaluate the robustness of the predicted system dynamics.
3) *We couple the insights from the reactive-flow simulations to a more comprehensive assessment of various hydrodynamic scenarios.* Specifically, drawing on tools and insights from the NRAP initiative, we use our reactive-flow results to develop reduced-order descriptions of the chemical and mineralogical evolution, which we then combine with an analysis of various flow conditions that could occur in the field.

Our analysis leads to several important conclusions related to the questions surrounding wellbore integrity:

a) *Self-sealing conditions arise over a wide range in cement properties and reservoir conditions.* Although some properties and conditions promote a stronger self-sealing response, self-sealing occurs for a wide range of Ca:Si ratios in cement and for various reservoir fluid compositions.

b) *Self-sealing conditions move along a wellbore proportional to the fluid velocity.* The chemical and mineralogical conditions for self sealing move at <10% the velocity of the moving fluid for low fluid:solid ratios. This result is particularly significant, as it leads to the ability to analyze the evolution of self-sealing in space and time.

c) *Self-sealing conditions can be maintained in a specific section of a wellbore for favorable hydrogeochemical conditions.* Specific factors that promote slow migration of the self-sealing reaction zone include high reservoir permeability, low reservoir overpressures, high calcium content in cement, and low fluid:solid ratios. Unfavorable hydrogeochemical conditions, however, can lead migration of the self-sealing reaction zone at a rate too high to promote sealing of a flow pathway.

d) *The phases produced by hydrating Portland cement (e.g., C–S–H and portlandite) represent a carbonic cement*. Portland cement is a hydraulic cement, meaning it sets and maintains integrity in the presence of water (paradoxically by being reactive with water). By analogy, the reaction products from hydrating cement are, in turn, carbonic cements, in that they set and maintain integrity in the presence of carbonic acid. The resulting phase assemblage is calcium carbonate and silica, which are the two phases responsible for sealing flow pathways in geologic processes and over geologic time. And, importantly, these phases are CO_2 resistant.

Introduction

Ensuring the long-term integrity of wellbores has been a central goal since the prospect of storing carbon dioxide (CO_2) in geologic reservoirs was seriously considered. Some early studies raised concern that the disequilibrium between acidic carbonated brines and basic hydrated Portland cement (hereafter referred to as "hydrated-cement") would result in complete dissolution of the seal in the annular region between casing and caprock (Scherer et al., 2005). Subsequently, numerous laboratory- and field-based studies have revealed the variety of alteration minerals that precipitate under realistic fluid:hydrated-cement ratios (see reviews by (Huet et al., 2011; Zhang and Bachu, 2011; Carey, 2013; Carroll et al., 2016), giving confidence that the chemical reactions between hydrated-cement and carbonated brine do not result in the complete removal of the seal under *static* fluid conditions. However, under *dynamic* (flowing) conditions (e.g., as would occur in an open channel or fracture in the cemented annular region), these chemical reactions become more complex, with some conditions leading to net precipitation but others leading to net dissolution. Whereas net precipitation can result in self-sealing of open flow pathways in the hydrated-cement, net dissolution could cause opening of the flow pathway. Hence, *ensuring the long-term wellbore integrity requires predicting how chemical reactions under flowing conditions evolve over space and time.*

Chemical reactions between hydrated-cement and carbonated brine include both diffusive alteration (e.g., Carey et al., 2007; Kutchko et al., 2007) and advectively controlled alteration along flow pathways (e.g., Carey et al., 2007, 2010; Duguid and Scherer 2010; Huerta et al., 2011; Huerta et al., 2013; Abdoulghafour et al., 2013, 2016; Mito et al., 2015; Wolterbeek et al., 2016). In both cases, the process can be viewed as dissolution and precipitation of minerals.

In the case of diffusion, the original mineralogy of the hydrated-cement is altered to form a new mineral assemblage that is in equilibrium with the carbonated brine. The alteration mineral assemblage depends on the composition of the hydrated-cement, carbonated brine, and caprock (e.g., Kutchko et al., 2007; Barlet-Gouédard et al., 2009; Kutchko et al., 2009; Carroll et al., 2011; Duguid et al., 2011; Kutchko et al., 2011; Scherer et al., 2011; Zhang et al., 2013; Verba et al., 2014; Mito et al., 2015), but the assemblage typically contains one or more calcium carbonate phases (calcite, aragonite, or vaterite) and a silica phase (usually amorphous). Other alteration phases that have been reported include Fe- and Mg-bearing carbonates, ettringite, various silicate and oxyhydroxide clay minerals, zeolites, and pyrite (Carroll et al., 2011; Kutchko et al., 2011; Scherer et al., 2011; Verba et al., 2014; Walsh et al., 2014).

In the case of advection, zones of carbonate and silica precipitation also form (Carey et al. 2007; Duguid and Scherer, 2010; Huerta et al., 2011). However, the spatio-temporal distribution of reactions varies relative to distance from the inlet of incoming fluid. In some regions, net dissolution occurs, whereas in other regions, net precipitation occurs, which can lead to a closing of flow pathways (a condition sometimes referred to as "self-sealing"). For long-term CO_2 storage, defining when and where self-sealing may occur is critical, as it can determine whether the integrity of a cemented wellbore is likely to improve or degrade over time in scenarios where an open flow pathway exists—e.g., a channel or crack in a cemented annulus or a delamination of the interface between hydrated-cement and caprock or casing (Gasda et al., 2004).

The nature of reactive-flow along open pathways in hydrated-cement has been the focus of numerous experimental and computational investigations. Brunet et al. (2016) recently synthesized these efforts into a conceptual model that defines regions of self-sealing and fracture-opening based on residence time and fracture aperture. In this model, the amount of time a specific volume of fluid remains in contact with the hydrated-cement determines whether it is in a state of net dissolution or net precipitation: initially a fluid-cement system exhibits net dissolution, but, as the compositions of the fluid and hydrated-cement evolve, the system will transition to net precipitation. Hence, Brunet et al. (2016) provides a basis for understanding the *temporal* distribution of self-sealing: Fluids must remain in contact with hydrated-

cement long enough to become saturated with respect to the sealing minerals (e.g., silica and/or calcium carbonate).

In this effort, we develop a conceptual model that focuses on the *spatial* and temporal distribution of self-sealing. The model complements the temporal model of Brunet et al. (2016). However, by focusing on where self-sealing occurs, we hope to provide a basis for understanding critical length scales needed to ensure the integrity of cemented wellbores for specific conditions. Ultimately, the two approaches focus on the same phenomena associated with the evolution of fluid composition as it interacts with hydrated-cement. In this context, the two approaches can be related through the relationship $t_R = L \bullet v_f^{-1}$, because the residence time (t_R) experienced by a moving volume of fluid at a specific distance (L) along the flow path depends on the fluid velocity (v_f). By recasting the analysis, we can focus on spatial aspects of self-sealing that are relevant to field parameters like length of a cemented section.

The conceptual model is developed using reactive-transport simulations of a system consisting of a simplified set of mineral phases: calcium-silicate-hydrate (C–S–H), portlandite, a silica phase, and calcite. The details of how a specific system will evolve will certainly be impacted by the myriad of other phases that could be present; however, we postulate that the general nature of a wellbore system can be understood through this simplified mineralogy because it dominates the system volumetrically and chemically. This postulate is consistent with other studies of the cement–brine system (as reviewed by Carroll et al. 2016).

We extend the previous studies by probing the impact of several uncertain or variable parameters. Although some computational studies have conducted limited sensitivity analyses (e.g., Abdoulghafour et al., 2016), we attempt to be more comprehensive relative to key mineralogical parameters: the calcium-to-silicon ratio of the C–S–H phase, poorly constrained thermodynamic relationships, and poorly constrained kinetic factors (i.e., rate constant and surface area).

Our goal is to define the spatial and temporal conditions for self-sealing. Clearly, the exact position in space and time will depend on the details of a specific wellbore, geology, fracture, etc. However, our motivation is to clarify the general principles that govern this system and to assess how these principles are impacted by variability in scenario-specific details and by uncertainties in key physical parameters (thermodynamics and kinetics). To achieve this goal, our simulation approach departs from those used in previous studies in several aspects, but most notably in the assumptions of constant velocity and of decoupled feedback between mineral reactions and permeability.

Constant Fluid Velocity

Underlying our analysis is the hypothesis that the spatial distribution of the boundary between opening and sealing is determined by fluid velocity. This hypothesis guided our calculations to focus on fluid velocity as a primary variable. In contrast, most previous studies have focused on fracture aperture as the primary variable, requiring assumptions on the relationship between aperture and permeability; several efforts have also tried to capture the dynamic nature between reaction and flow, requiring additional assumptions on the relationship between ΔV_{solids} and aperture/permeability. Our calculations avoided these assumptions by assuming constant fluid velocities. Although our assumption does not mimic actual dynamic scenarios in which flow rate, aperture, and permeability are all coupled and changing over time, it nevertheless does facilitate understanding the innate controls on the system. An additional difference in our approach to fluid velocity is to focus on actual fluid velocity (m/s) as opposed to an operational parameter that might be measured experimentally (e.g., ml/min); by emphasizing actual fluid velocity, we exploit a parameter that is scale independent.

One might question whether the use of constant velocity is reasonable, as it does not mimic most (any?) real field conditions (albeit it does accurately capture the physics that govern the system). In fact, this approach is entirely consistent with conventional analyses based in both experiments and theory. An

experimental analogy is the use of constant pressure or constant velocity in a flow-through experiment. In real situations, velocity and pressure vary spatially and temporally, so these experiments do not accurately mimic a specific scenario. Instead, these experiments control velocity or pressure in order to isolate coupled effects, recognizing that the exact behavior of a real system is impacted by these coupled effects. By analogy to a theoretical treatment, our use of constant fluid velocity is akin to analysis of partial derivatives to assess the influence of specific key variables. As with these examples, our use of constant velocity does not compromise the physics; rather, it enables isolation of variables.

Decoupled Feedback between Precipitation and Permeability

Our analysis also departs from other computational studies of self-sealing in that it does not contain feedback between mineral reactions and permeability. This feedback clearly governs the behavior of a real system, inasmuch as mineral reactions can change porosity, which in turn can impact flow; indeed, that is the essence of self-sealing. Thus, in a real system, as mineral precipitation begins to close a flow pathway, fluid velocity will slow, altering the distribution of subsequent chemical reactions. This coupling can lead to an acceleration of sealing under a precipitation condition (and, conversely, it can lead to an acceleration of opening in a dissolution condition).

Our rationale behind decoupling precipitation and permeability in our analysis is twofold: first, it is central to our constant velocity approach, and second, it eliminates the need to adopt significant additional assumptions. This latter is particularly challenging from both a computational and observational standpoint. The conventional approach to this coupling is to assume a relationship between porosity and permeability, as is typically done in using field data on porosity to infer reservoir permeability. However, as is well known, the measured relationship between porosity and permeability is qualitative, with data from field cores showing extensive scatter (orders of magnitude). This lack of a well-defined empirical relationship introduces significant uncertainty into any assumed relationship embodied in a reactive-flow simulation. We avoid this uncertainty in our analysis. Nevertheless, our analysis remains applicable to realistic scenarios because we explicitly assess the relationship between fluid velocity and reaction; hence, with an appropriate formulation for coupling changes in porosity to changes in permeability, one can use the relationships we derive to simulate a specific scenario exactly. For example, one could simulate where precipitation would occur along a fracture with heterogeneous apertures, or exactly where and when a specific flowpath would seal.

In general, applying our analysis in the absence of dynamic feedback between precipitation and permeability is conservative under a precipitation scenario and optimistic under a dissolution scenario.

Extension to Implications

An ultimate goal is to develop a scientific basis for answering two questions facing CO_2 storage operations: First, what is a sufficient quantity of cement to maintain integrity over the design life of a project? Second, what makes a cement "compatible" with a carbonated brine? These questions are central to US EPA defined Class VI well permitting considerations.

Our analysis addresses this first question by revealing the underlying mechanisms of sealing and by defining a zone in which these mechanisms operate. This zone does not guarantee that self-sealing will occur, which requires a consideration of the size of flowpath that must be sealed. Rather, the "sealing-reaction zone" is the only region in which conditions exist that promote the precipitation reactions required for sealing. Our analysis lays the basis for evaluating where this zone occurs in space and time, identifying and quantifying three primary factors (fluid velocity, time, and fluid:solid ratio) and several secondary factors (including the composition of hydrated calcium silicate hydrate, portlandite content, rates of reaction, composition of the reservoir brine, and temperature). We use these relationships to explore the implications of fluid velocity and self-sealing in the context of risk assessment. Specifically, we use fluid

velocity to identify field scenarios consistent with either self-sealing or fracture opening: Pathways with a sufficiently low velocity should self-seal, whereas those with an unfavorably high velocity could lead to net dissolution and fracture opening at a specific length scale. Hence, we explore various controls on fluid velocity, including fracture aperture, permeability in the reservoir, permeability in the overlying unit into which the fluid flows, or the magnitude of the pressure drive between the reservoir and overlying unit.

We address the second question by considering the nature of the dissolution and precipitation reactions that occur when a hydrated Portland cement interacts with carbonated brine. In addition to driving self-sealing, these reactions lead to a conversion of hydrated Portland cement—which consists largely of hydrated calcium silicate (or C–S–H) and portlandite—to a mixture of calcium carbonate and silica. These end products are stable in the presence of carbonated brine, so the new material within the wellbore annulus will maintain integrity, i.e., it is CO_2 resistant.

For both questions, we are focused on one of three possible scenarios for wellbore leakage: the leakage of CO_2 charged brine. Two other endmember scenarios are also possible in a CO_2 storage operation. A well may leak pure CO_2 and/or another gas; or a well may leak pure brine. Our intent is not to disregard these other scenarios. Rather, we focus on CO_2-charged brine because it is at the root of the concerns that wellbore integrity may be compromised by acidic brine (i.e., it is the driver behind the focus on CO_2 resistant cements).

Methods

Several recent efforts have developed similar reactive-transport models for this system (Carey et al. 2007; Carey and Lichtner 2007; Blanc et al., 2010; Brunet et al., 2013; Zhang et al., 2013; Abdoulghafour et al., 2016; Brunet et al., 2016; Huerta et al., 2016; Tremosa et al., 2017), using a variety of simulation codes, thermodynamic representations, and kinetic models. In this effort, we build on a kinetic and thermodynamic model we developed for acid-base alteration of hydrated-cement and silica-rich aggregates (Guthrie and Carey, 2015). However, we also consider the variability and uncertainty embodied in the various thermodynamic and kinetic models in our analysis of the nature of the predicted reactions.

Although cement can contain a variety of phases in the system Ca-Si-Al-Fe-S-H-O-Cl (including both hydrated-cement phases and unhydrated-cement phases), our model only considers calcium-silica-hydrate (C–S–H) and portlandite. These are typically the volumetrically dominant phases in hydrated-cement and are very reactive, hence, their behavior has a major impact on the integrity of cemented wellbores. Our model also simplifies the alteration mineralogy by considering only calcite and amorphous silica. This simplification still captures the dominant alteration mineral assemblage that has been observed both in the lab and field. The one caveat to this lies in the exclusion of other calcium carbonate phases that have been observed in carbonation of hydrated-cement (e.g., vaterite, aragonite, and hydrated calcium carbonates). These other calcium carbonate phases can be kinetically favored under these conditions, so our focus on calcite represents a conservative assumption relative to self-sealing. We also note that some studies have identified other silica-rich amorphous phases in the alteration assemblage (e.g., an amorphous material with a mordenite-like local atomic structure, as reported by Mason et al., 2013, based on $^{27}Al\{^{1}H\}$ REDOR NMR). Although inclusion of such alteration phases would improve the exactness of our model, we believe it is not essential relative to elucidating the nature of the chemical and mineralogical phenomena that govern the dynamics of the system. Indeed, if an alternative silica-rich amorphous phase is thermodynamically and/or kinetically favored over the amorphous silica assumed here, it would precipitate even earlier than what we predict below (i.e., our assumption is, hence, conservative). Yet inclusion of such material would require expanding the chemical components in the system, adding complexity that might obscure the essence of the system dynamics. And, it would require additional uncertainties and assumptions on the thermodynamics and kinetics. Thus, we have chosen to focus on a simpler system.

Computational

The simulation code PFLOTRAN was used to perform reactive-transport calculations (Hammond et al., 2012; Lichtner et al., 2014, 2017). PFLOTRAN is an open source, state-of-the-art massively parallel subsurface flow and reactive transport code that solves partial differential equations describing multiphase, multicomponent, and multiscale reactive flow and transport in porous materials. The code is a continuum-scale simulator based on Darcy-flow physics. However, it was run in constant fluid-velocity mode, which bypasses the need to define permeability for the system. The assumption of constant fluid velocity does not mimic most real scenarios where dissolution, precipitation, and geomechanics may be changing the fracture aperture dynamically, but it does avoid the need to make uncertain assumptions about permeability. Furthermore, it does not compromise our analysis of the distribution of reactions in space and time as a function of fluid velocity.

Simulations were 1D and assumed isothermal conditions. For validation runs, we assumed transport by diffusion only to compare with experiments by Kutchko et al. (2007); however, all other runs assumed transport by advection only. As a 1D continuum, these calculations did not attempt to simulate an open fracture and a fracture face, discretely. Instead, each node contained both fluid and solid, representing a case where the representative elementary volume (REV) included both a fluid-filled fracture and a mineral-bearing fracture face (Fig. 1). In most cases, the ratio of fluid

to solid was 0.25; but the fluid:solid ratio is a primary variable in the reaction dynamics, so additional simulations were conducted varying it in order to derive this relationship.

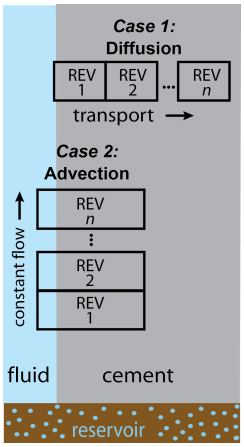

Figure 1. Schematic diagram showing representative elementary volumes (REVs) used in the simulations

Implicit in our use of 1D for the advection cases is that diffusion within the fluid is insignificant under these conditions. Indeed, for the fluid velocities we explored (10^{-5}–10^{-1} m s^{-1}), Péclet numbers are generally much greater than 1. For example, at the mid-velocity range, Pe>1 for apertures as small as ~1 µm, and even at the low velocity end we explored, Pe>1 for apertures >~100 µm. Hence, our focus on advection-dominated transport in the fluid is valid (except in considering the detailed behavior of small apertures).

Our focus on 1D also precludes the ability to resolve spatial variation in the reaction, as might occur along a real fracture. Neglecting to address these spatial aspects directly is also valid for two reasons: first, spatial variation due to aperture variability is implicitly addressed by our focus on fluid velocity; in other words, we explore a range of fluid velocity that is sufficient to capture the various dynamics that would occur along a fracture with varying aperture and, hence, varying fluid velocity. Second, spatial variation due to mineralogical variability in the cement along a fracture is already assumed to be negligible by our assumption of continuum behavior. This assumption likely holds because the grain size of hydrated-cement is significantly smaller than the length scale for apertures of concern; experimental studies appear to confirm this assumption, as spatial variations of sealing phenomena are at a larger scale than hydrated-cement grain size (e.g., Huerta et al., 2011, 2013; Abdoulghafour et al., 2016).

Thermodynamics

Simulations assumed equilibrium aqueous geochemistry. The basis set of aqueous species for the simulations included H^+, Na^+, Ca^{2+}, H_4SiO_4, HCO_3^-, and Cl^-. The secondary aqueous species considered are given in Table 1. The equilibrium constants used to represent the aqueous speciation reactions for these secondary species were taken from the Thermoddem database, which has been described by Blanc et al. (2012). This database has been developed to allow predictions of fluid–mineral reactions for a variety of energy and environmental applications. The database is maintained by the Bureau de Recherches Géologiques et Minières (BRGM), the French geological survey.

For silica, only monomeric species were included in the calculations. Due to lack of appropriate thermodynamic and/or experimental data, we did not account for larger polymeric silica phases nor for silica sols (both of which can form at high pH). Their inclusion would have raised the value of aqueous silica concentration in the higher pH regions, and they can impact precipitation rates and mechanisms (especially at high pH). Nevertheless, their omission in this study is unlikely to impact the primary conclusions relative to order-of-magnitude chemical behavior of the system; nor should it impact our analysis of the initiation of net precipitation, which occurs at in a mid-pH range where the concentrations of these species should be negligible.

An extended Debye-Hückel formulation was used for the activity coefficients. Ionic strengths (I) remained below 0.08 for both the low and high pH regions of the simulations, except for the sodium chloride runs (for which I≈2 for the incoming fluid). In this latter case, the simulations should still provide adequate insight into the chemical impact of dissolved NaCl, albeit they are not rigorously accurate.

Dissolved CO_2 values were made consistent with the values reported by (Duan and Sun 2003) by calibrating fugacity to use with the equilibrium for CO_2(g) given in Table 1. Details are provided in Appendix I.

Mineral dissolution reactions are given in Table 2. Solubility products for portlandite, amorphous silica, and calcite were taken from BRGM's Thermoddem database (Blanc et al., 2012). Three sets of solubility products were considered for the primary phase in hydrated-cement (calcium silicate hydrate or C–S–H). One set consisted of the three compositions of C–S–H as reported by BRGM (Blanc et al., 2012), and one set was the two compositions reported by Kulik and Kersten (2001). The third set of solubility products for C–S–H was derived from the solid solution model developed by Carey and Lichtner (2007); Carey and Lichtner report solubility constants at 25 °C, and these were used along with the Van 't Hoff equation to extend their model to elevated temperatures (details provided in Appendix I).

Table 1

Speciation Reactions for Secondary Aqueous Species[†]

Reaction	$\log(K_{sp})_{25°C}$	$\log(K_{sp})_{60°C}$	$\log(K_{sp})_{100°C}$	Molecular Weight ($g\ mol^{-1}$)
$OH– + H^+ \rightarrow H_2O$	14.0025	13.0341	12.2619	17.0073
$CaOH^+ + H^+ \rightarrow Ca^{2+} + H_2O$	12.7810	11.3717	10.1045	57.085
$HSiO_3^- + H^+ + H_2O \rightarrow H_4SiO_4$	9.8190	9.3439	9.0343	77.092
$H_2SiO_4^{2-} + 2H^+ \rightarrow H_4SiO_4 + 2H_2O$	23.2700	21.9786	20.9797	94.099
$NaOH_{(aq)} + H^+ \rightarrow Na^+ + H_2O$	14.7510	13.7622	12.8514	39.997
$HCl_{(aq)} \rightarrow H^+ + Cl^-$	0.7100	0.8523	0.8054	36.460
$CO_{2\,(g)} + H_2O \rightarrow H^+ + HCO_3^-$	–7.8264	–8.0640	–8.3674	44.01
$CaCO_{3\,(aq)} + H^+ \rightarrow Ca^{2+} + HCO_3^-$	7.1070	6.5806	6.1187	100.087
$CaHCO_3^+{}_{(aq)} \rightarrow Ca^{2+} + HCO_3^-$	–1.1030	–1.0385	–1.1718	101.095
$CO_{2\,(aq)} + H_2O \rightarrow H+ + HCO_3^-$	–6.3543	–6.2796	–6.3935	44.01
$CO_3^{2-} + H^+ \rightarrow HCO_3^-$	10.3268	10.1272	10.0798	60.009
$NaCO_3^- + H^+ \rightarrow Na^+ + HCO_3^-$	9.0570	8.0976	7.2174	82.999
$NaHCO_{3\,(aq)} \rightarrow Na^+ + HCO_3^-$	0.2470	0.4633	0.6770	84.007

[†] Data from the Thermoddem database (http://thermoddem.brgm.fr) as described in Blanc et al. (2012).

Table 2. Mineral Dissolution Reactions

Reaction	log(K_{sp}) 25°C	log(K_{sp}) 60°C	log(K_{sp}) 100°C	Molecular Weight (g/mole)	Molar Volume (cm^3/mole)	Reference
$Ca(OH)_{2\ (portlandite)} \rightarrow Ca^{2+} + 2OH^-$	22.8120	20.4285	18.2713	74.093	33.056	A
$SiO_{2\ (am)} + 2H_2O \rightarrow H_4SiO_4$	–2.7024	–2.4523	–2.2240	60.084	29.000	A
$CaCO_{3\ (calcite)} + H^+ \rightarrow Ca^{2+} + HCO_3^-$	1.8487	1.3387	0.7856	100.087	36.934	A
$Ca_{1.70}SiO_{3.70}{\cdot}1.70H_2O + 3.40H^+ \rightarrow 1.70Ca^{2+} + H_4SiO_4 + 1.40H_2O$	30.63	27.87	25.36	186.246	94.397	B
$Ca_{1.67}SiO_{3.67}{\cdot}2.10H_2O + 3.34H^+ \rightarrow 1.67Ca^{2+} + H_4SiO_4 + 1.77H_2O$	29.13	26.03	23.22	201.59	73.1	C
$Ca_{1.63}SiO_{3.63}{\cdot}1.63H_2O + 3.26H^+ \rightarrow 1.63Ca^{2+} + H_4SiO_4 + 1.26H_2O$	29.03	26.43	24.06	180.976	92.584	B
$Ca_{1.60}SiO_{3.60}{\cdot}2.58H_2O + 3.20H^+ \rightarrow 1.60Ca^{2+} + H_4SiO_4 + 2.18H_2O$	28.0022	25.5919	23.4754	196.288	84.68	A
$Ca_{1.50}SiO_{3.50}{\cdot}1.50H_2O + 3.00H^+ \rightarrow 1.50Ca^{2+} + H_4SiO_4 + 1.00H_2O$	26.10	23.79	21.69	171.225	89.230	B
$Ca_{1.38}SiO_{3.38}{\cdot}1.38H_2O + 2.76H^+ \rightarrow 1.38Ca^{2+} + H_4SiO_4 + 0.76H_2O$	223.46	21.32	19.37	162.405	86.195	B
$Ca_{1.27}SiO_{3.27}{\cdot}1.27H_2O + 2.54H^+ \rightarrow 1.27Ca^{2+} + H_4SiO_4 + 0.54H_2O$	21.10	19.20	17.46	154.386	83.436	B
$Ca_{1.20}SiO_{3.20}{\cdot}2.06H_2O + 2.40H^+ \rightarrow 1.20Ca^{2+} + H_4SiO_4 + 1.26H_2O$	19.3013	17.7043	16.3119	164.489	71.95	A
$Ca_{1.17}SiO_{3.17}{\cdot}1.17H_2O + 2.34H^+ \rightarrow 1.17Ca^{2+} + H_4SiO_4 + 0.34H_2O$	18.96	17.28	15.74	147.065	80.917	B
$Ca_{1.08}SiO_{3.08}{\cdot}1.08H_2O + 2.16H^+ \rightarrow 1.08Ca^{2+} + H_4SiO_4 + 0.16H_2O$	17.03	15.55	14.19	140.354	78.606	B
$Ca_{0.92}SiO_{2.92}{\cdot}0.92H_2O + 1.84H^+ + 0.16H_2O \rightarrow 0.92Ca^{2+} + H_4SiO_4$	13.67	12.54	11.51	128.479	74.521	B
$Ca_{0.83}SiO_{2.83}{\cdot}1.30H_2O + 1.66H^+ \rightarrow 0.83Ca^{2+} + H_4SiO_4 + 0.13H_2O$	11.15	10.07	9.09	136.84	51.7	C
$Ca_{0.80}SiO_{2.80}{\cdot}1.54H_2O + 1.60H^+ \rightarrow 0.80Ca^{2+} + H_4SiO_4 + 0.34H_2O$	11.0503	10.1962	9.4609	132.690	59.29	A
$Ca_{0.79}SiO_{2.79}{\cdot}0.79H_2O + 1.58H^+ + 0.42H_2O \rightarrow 0.79Ca^{2+} + H_4SiO_4$	10.87	10.05	9.29	118.302	71.020	B

A: From the Thermoddem database (http://thermoddem.brgm.fr) as described in Blanc et al. (2012).

B: From (Carey and Lichtner 2007), adapted to high temperature using the Van 't Hoff equation and a ΔH determined by regression of ΔH values vs. Ca:Si ratio as reflected in data given by Kulik and Kersten (2001) and Blanc et al. (2012); linear regression gave the equation ΔH (kJ/mole) = –120.10xCa:Si + 49.58.

C: Derived from (Kulik and Kersten 2001) using data provided in their Table IV for logK; molecular weight was calculated by stoichiometry.

Figure 2 shows a comparison of these various models for congruent dissolution of C–S–H in water at 60 °C. As can be seen, the models of Blanc et al. (2012) and Carey and Lichtner (2007) predict relatively similar fluid chemistry at saturation. However, the model of Kulik and Kersten (2001) predicts slightly lower values for total dissolved silica and calcium as well as slightly lower values of pH. (The smaller apparent impact on pH is, of course, to be expected, as pH reflects logarithmic changes in concentration of hydrogen ion.) Despite the similarities in behavior for congruent dissolution, as will be shown below, the three models behave differently relative to self-sealing implications under advective conditions. All predict self-sealing to occur, but the Carey and Lichtner (2007) model predicts the least amount of net-volume increase (i.e., it is the most conservative). Hence, we use the Carey and Lichtner model for our base case analysis in order to provide a set of minimum conditions for self-sealing.

Simulations of the solubility experiments reported by (Greenberg and Chang, 1965) were used as an additional assessment of the behavior of the C–S–H models. (Greenberg and Chang data were chosen for comparison because they were also used by Kulik and Kersten as a benchmark.) Greenberg and Chang (1965) noted their experiments reflected incongruent dissolution (because the aqueous Ca:Si ratios differed from those in dissolving solids); to account for this, our simulations used a starting calcium concentration adjusted such that the final calcium concentrations were comparable to those reported by Greenberg and Chang. Figure 3 shows the comparison of the experimental values from Greenberg and Chang with the calculated values based on the various models. Calculated values for total dissolved calcium (shown as pCa, or –log[Ca]) match well with experiment, as expected since they were adjusted to match. However, calculated values for pH and for total dissolved silica (shown as pSi) provide an indication of how the three C–S–H solubility models compare with one another and with the experimental data. Values for pH compare well, both among the models and with the experiments, with the largest deviations with the experiments occurring at low values of Ca:Si. In the case of dissolved silica, the deviations are somewhat larger, both with experiments and among the models. In general, the Carey and Lichtner model predicts higher dissolved silica than the other two models, but that model provides a good match with the experimental data, as does the model reported by Blanc et al. (2012). The Kulik and Kersten (2001) model deviates slightly from the experimental model, predicting a lower value of total dissolved silica (i.e., a higher value of pSi). At higher Ca:Si, all of the models predict lower values of total dissolved silica than the values reported by Greenberg and Chang. As noted above, we did not consider any aqueous silica polymers in the simulations, which likely accounts for this discrepancy (given that polymers become significant at higher pH). This discrepancy is likely to have minimal impact on the interpretations below, because the simulations all considered an excess of C–S–H (i.e., the solubility of silica was not limited by amount of dissolving material).

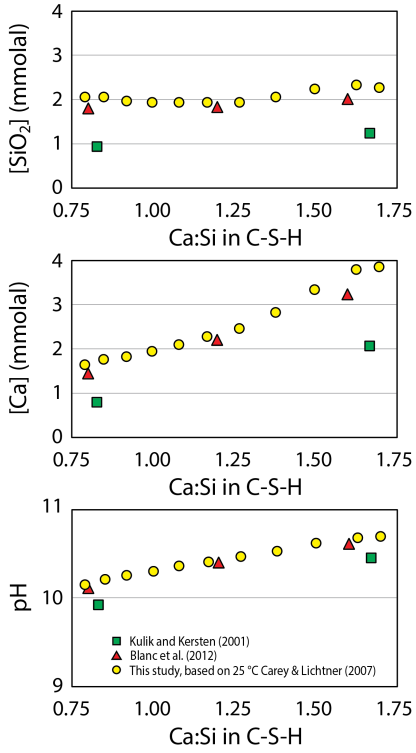

Figure 2. Plots of solution chemistries simulated for congruent dissolution of each of the C–S–H models considered in the study. Simulations were conducted at 60 °C in pure water.

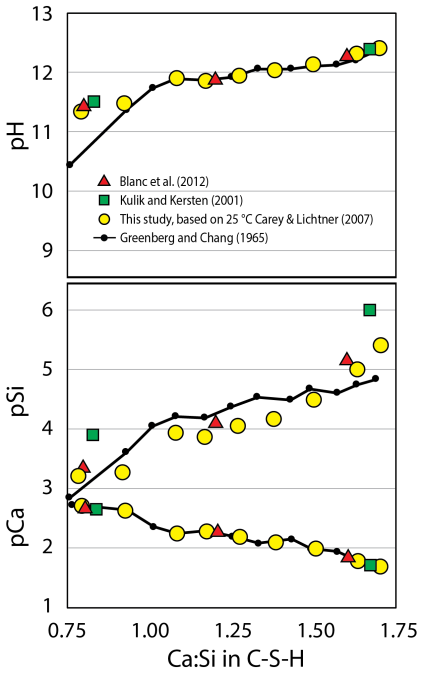

Figure 3. Comparison of calculated fluid chemistries with experimental values observed by Greenberg and Chang (1965).

Kinetics

Mineral dissolution was modeled (Lichtner, Hammond et al. 2017) using a kinetic rate law assuming mineral-surface-controlled behavior consistent with transition state theory:

$$r_{m,T} = -A_m \left(\sum_l k_{m,T,l}\, P_{m,l}\right)\left(1 - \frac{Q_m}{K_{m,T}}\right)^{\frac{1}{\sigma_m}} \qquad (1)$$

where:

- $r_{m,T}$ is the rate (mol m–3 s–1) at which (in the case of dissolution) components are released from mineral *m* at temperature *T*;
- A_m is the surface area ($m^2\ m^{-3}$) for mineral *m*;
- Σ_l indicates a sum over the *l* parallel dissolution reactions for mineral *m*;
- $k_{m,T,l}$ is the mineral's dissolution rate (mol m^{-2} s^{-1}) for mechanism *l* at the temperature of interest (see Eq. 2);
- $P_{m,l}$ is the prefactor for the l^{th} parallel reaction (see Eq. 3);
- Q_m denotes the ion activity product relative to mineral *m*;
- $K_{m,T}$ is the solubility product for the mineral at temperature T; and
- σ_m is the Temkin's constant for dissolution of mineral *m*, which was assumed to be 1 in this study.

The temperature corrected dissolution rate is given by:

$$k_{m,T,l} = k^0_{m,l} \exp\left[\frac{E_{m,l}}{R}\left(\frac{1}{T_0} - \frac{1}{T}\right)\right] \qquad (2)$$

where:

- $k^0_{m,l}$ is the mineral's dissolution rate (mol m^{-2} s^{-1}) for mechanism *l* at the reference temperature (T_0) (taken to be 25 °C or 298 K in this study);
- $E_{m,l}$ is the activation energy (J mol^{-1}) for the mineral's dissolution reaction; and
- *R* is the gas constant (8.314 J mol^{-1} K^{-1}).

The prefactor in equation 1 describes the dependence of the l^{th} dissolution reaction for mineral *m* relative to the activity of various species in the fluid and it is given by:

$$P_{m,l} = \prod_i a_i^{\alpha_{i,l,m}} \qquad (3)$$

where:

- $\alpha_{l,l,m}$ is the reaction order with respect to the activity *a* of species *i* in the context of the l^{th} dissolution reaction mechanism for mineral *m*; and
- Π_i denotes a product over the *i* species, which could include both primary and secondary species.

In this study, the only aqueous species for which a species-dependent dissolution mechanism was considered was H^+, which was used in the treatment of dissolution for C–S–H, portlandite, and calcite.

The ratio of the ion activity product, Q_m, and solubility product, $K_{m,T}$, is a measure of how close the system is to equilibrium with the mineral, *m*. At equilibrium, this ratio is 1, and the third factor in the rate equation (1) is zero (i.e., the rate becomes zero). The log of this

ratio is often referred to as the saturation index, SI. When SI is positive, a fluid is supersaturated with respect to mineral *m*, so the mineral will precipitate; when SI is negative, a mineral will dissolve.

As noted, several recent efforts have developed kinetic models for this system (Blanc et al., 2010; Brunet et al., 2013; Zhang et al., 2013; Abdoulghafour et al., 2016; Brunet et al., 2016; Huerta et al., 2016; Tremosa et al., 2016), and each has used a different set of values for *k* and *A*. The maximum effective rates ($r_{max}=k_T \cdot A$) are compared in Fig. 4, where log[*r*] is shown as a function of pH. (In this case, r consists of the first two factors in Eq. 1.) Several observations can be made from these plots. First, the dissolution/precipitation rates of amorphous silica and C–S–H are likely to be significantly slower than those for calcite and portlandite. Second, the rates used in various studies for portlandite, C–S–H, and amorphous silica vary over orders of magnitude. In the case of amorphous silica, the rates used in this study—as reported by Palandri and Kharaka (2004) for precipitation of amorphous silica—are comparable to those used by Abdoulghafour et al. (2016) but more than an order of magnitude higher than those used by Brunet et al. (2016). For portlandite and C–S–H, the spread is even higher. In the case of portlandite, our base-case rates are intermediate to those used by Bullard et al. (2010) and Abdoulghafour et al. (2016) on the high side and Zhang et al. (2013) and Brunet et al. (2016) on the low side. For C–S–H, we use the rates reported by Marty et al. (2015), which are higher by 1–3 orders of magnitude than those used by Guthrie and Carey (2015), Zhang et al. (2013), Baur et al. (2004), Abdoulghafour et al. (2016), and Brunet et al. (2016). Finally, for calcite the base case scenarios use the model presented by Palandri and Kharaka (2004), which is about an order of magnitude faster than the model of Marty et al. (2015) over most of the region; the biggest discrepancy, however, occurs in the low pH regions where the pH-dependent model of Palandri and Kharaka becomes very rapid relative to the model of Marty et al. Because of these wide discrepancies, we consider the dissolution rate to be a highly uncertain parameter so we assess the impact of this uncertainty in our analysis. Table 3 shows the values used in this study for $k_{25°C}$ and *A*, including both the base case and the range in *A* assessed in the analysis. In general, our base-case rates are comparable to those used by Tremosa et al. (2016) for their simulations at 50 °C.

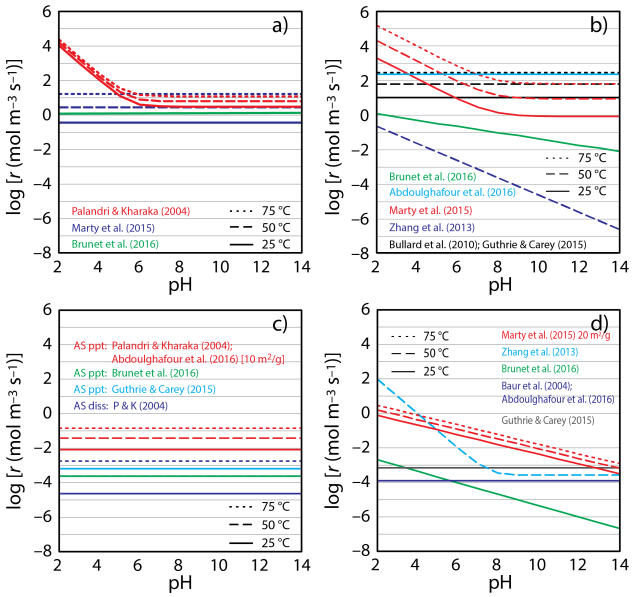

Figure 4. Plots of release rates (moles of mineral released per m^3 of mineral per second) for various minerals considered in the model simulations: (a) calcite, (b) portlandite, (c) amorphous silica, and (d) C–S–H. Curves correspond to studies described in the text. The red curves indicate the kinetic models used for the base-case simulations.

Table 3. Dissolution rate parameters used in this study

Mineral		Acid Mechanism			Neutral Mechanism		
		$\log[k_{25\,°C}]$ (mol m^{-2} s^{-1})	ΔH (kJ mol^{-1})	α_{H+}	$\log[k_{25\,°C}]$ (mol m^{-2} s^{-1})	ΔH (kJ mol^{-1})	Surface Area (m^2 m^{-3})
Calcite	Base	–0.30	14.4	1.0	–5.81	23.5	1.9×10^6
	Range						Marty et al. (low) 1xbase (high)
Portlandite	Base	–3.10	75.0	0.6	–7.66	75.0	3.7×10^7
	Range						0.001xbase (low) 10xbase (high)
Amorphous Silica	Base	—	—	—	–9.42	49.8	2.1×10^7
	Range						0.01xbase (low) 1xbase (high)
C–S–H	Base	–7.23	23.0	–0.28	—	—	4.6×10^7
	Range						0.001xbase (low) 1xbase (high)

Observations

Validation Case: Diffusive Alteration

To assess the validity of the thermodynamic and kinetic model, we simulated the experiment of Kutchko et al. (2007), which involved exposing a Class H Portland-based cement to CO_2-charged brine for 9 days at 50 °C and 30 MPa. Kutchko et al. pre-cured the Portland cement for 28 days, and the resulting hydrated paste contained a mixture of phases, including C–S–H, portlandite, unhydrated-cement, and likely a range of other minor phases. In our simulations, however, we focused only on a simplified system of C–S–H and portlandite, which were observed by Kutchko et al. to be central to the alteration reactions. They also observed the formation of amorphous silica and calcium carbonate as the major alteration assemblage. So, our model captures the primary phases involved in their experiments.

In our validation runs, the only tuned parameter was tortuosity, which was set to 0.005 to reproduce an alteration depth comparable to that observed in the experiments. (The diffusion coefficient for all aqueous species was set to 10^{-9} m^2 s^{-1}.)

These validation runs demonstrated:

- The thermodynamic and kinetic model we use captures the key aspects of the fluid–mineral reactions that result from diffusive alteration of hydrated Portland cement by carbonated brine.
- Two of the thermodynamic models (Carey and Lichtner, 2007; Blanc et al., 2012) predict textural features observed experimentally and in field samples (e.g., relative ΔV of carbonated and hydrated cements as well as the development of a zone of increased porosity); one of the thermodynamic models (Kersten and Kulik, 2007) predicts larger decreases in porosity than observed when hydrated cement is carbonated.
- The mineralogical and textural observations are reproduced over the kinetic uncertainty range for calcite and portlandite; dissolution rates for amorphous silica and C–S–H that are significantly lower than our base-case rates predict mineralogical and textural changes that differ from those observed by Kutchko et al.

Base Case (Carey & Lichtner C–S–H Model)

As noted, our base case assumed the thermodynamic model of Carey & Lichtner and the dissolution rates shown as red curves in Fig. 4.

Our base-case simulations for the Kutchko et al. experiments are shown in Figure 5.

Our base-case kinetic and thermodynamic model reproduces the mineral assemblage observed in the experiments, moving from unaltered hydrated-cement (at distances greater than ~425 μm) to a portlandite-depleted zone (at a distance equal to ~400 μm), then to a calcite-plus-silica zone (from ~50 μm to ~350 μm), and ultimately to a silica-only zone at the surface (10–50 μm). The calcite-plus-silica zone shows a slightly larger volume than the hydrated-cement, implying a reduction in porosity, as seen in the experiments. (Kutchko et al. describe the silica-only zone as a "porous silica"; the silica volume shown in Figs. 5–7 assumes a dense silica, so it's volume appears lower.)

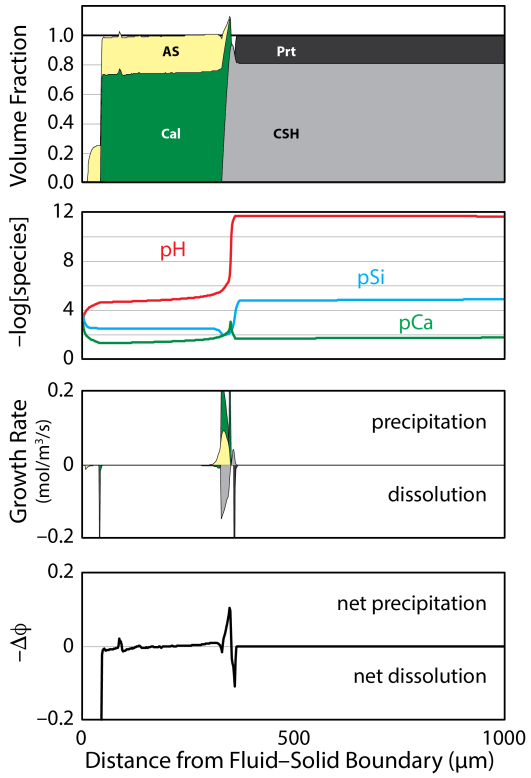

Figure 5. Simulation of the diffusive alteration observed in the experiments of Kutchko et al. (2007) assuming the Carey and Lichtner C–S–H model with a Ca:Si ratio of 1.63. This Ca:Si ratio was chosen because it is has a logK comparable to those for the Kulik and Kersten and Blanc et al. C–S–H models with Ca:Si ratios of 1.67 and 1.60, respectively (see Fig. A-I.7). The sample surface started at 0 μm (at the left) with higher values on the x-axis progressing into the sample interior.

Figure 5 also shows details of the reaction front progression. The alteration zone coincides with a pH gradient at the transition from the acidic altering fluid to the basic fluid in equilibrium with the hydrated-cement. This is best illustrated by the plot of the growth rate for minerals, which shows three geochemical zones. The first zone is defined by the system calcite+silica+C–S–H, with C–S–H dissolving and calcite and amorphous silica precipitating. The second zone (down gradient from zone 1) is defined by calcite+C–S–H, with both C–S–H and calcite precipitating; the pH increases sharply in this zone. These two geochemical zones coincide with a pronounced decrease in porosity (shown as an increase in $-\Delta\phi$ in Fig. 5) at ~380 μm from the boundary between the solid and the altering fluid. Between these zones of decreased porosity and the pristine hydrated-cement is a third zone of increased porosity reflecting removal of portlandite, which has also been observed experimentally (Kutchko et al., 2007).

Alternative Thermodynamic Models

Figures 6 and 7 show similar alteration patterns predicted using the C–S–H thermodynamic models from Blanc et al. (2012) and Kulik and Kersten (2001).

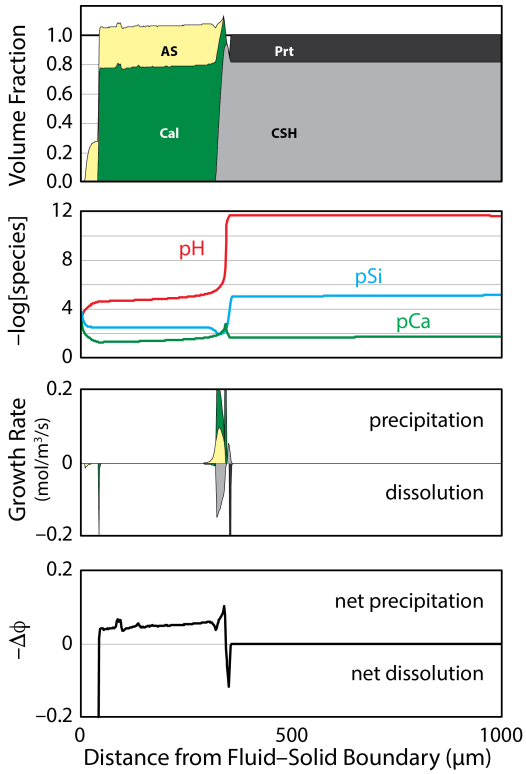

Figure 6. Simulation of the diffusive alteration observed in the experiments of Kutchko et al. (2007) assuming the Blanc et al. C–S–H model with a Ca:Si ratio of 1.60.

In general, these models predict a similar alteration pattern to the model based on Carey and Lichtner, including the coincidence of dissolution and precipitation with the pH gradient, and a zone of increased porosity due to portlandite dissolution. One noticeable difference, however, is in the predicted volume

change in the zone of calcite and amorphous silica. Whereas the Carey and Lichtner model predicts only a slight volume increase throughout most of the calcite+silica zone (slight "net precipitation" in Fig. 5), the other two models predict a significant volume increase throughout this zone. The Kulik and Kersten model, in particular, has a notable volume increase in this zone. (As noted above, our model intentionally omits the dynamic feedback between precipitation/dissolution and permeability, which can accelerate or decelerate fluid movement; hence, these various models can be compared directly in the context of reaction dynamics, without confounding by the coupled processes.)

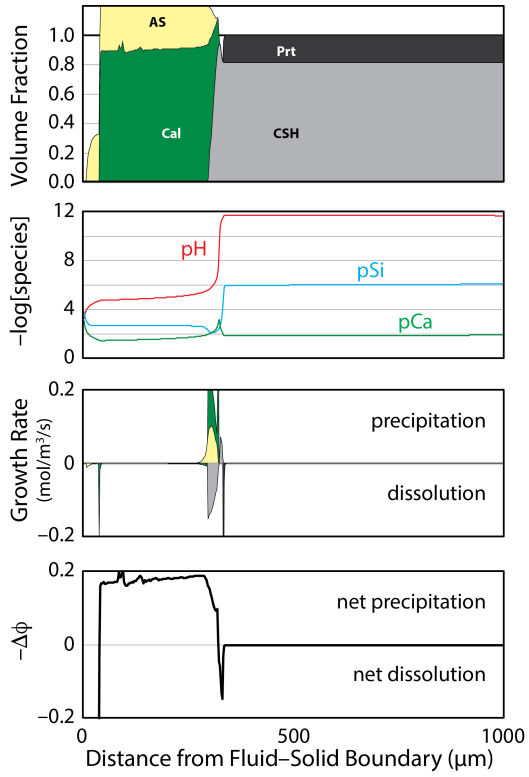

Figure 7. Simulation of the diffusive alteration observed in the experiments of Kutchko et al. (2007) assuming the Kulik and Kersten C–S–H model with a Ca:Si ratio of 1.67.

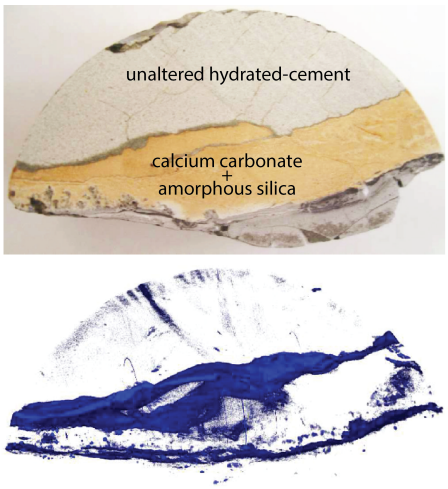

Figure 8. Sample of altered hydrated-cement recovered from SACROC CO_2-EOR reservoir (after Carey et al., 2007). Upper image shows orange zone of diffusively altered hydrated-cement. Lower image shows X-ray CT image highlighting regions of higher density (shown in blue).

Although Kutchko et al. (2007) do not comment specifically on relative porosities in the unaltered hydrated-cement and carbonate+silica zone, a qualitative assessment of their SEM images does not support a significant volume change. This conclusion is also consistent with a sample of diffusively altered hydrated-cement from a CO_2-EOR reservoir as reported by Carey et al. (2007) (Fig. 8). Computed X-ray tomography of the alteration zone shows a comparable to slightly higher density in the carbonate+silica zone relative to unaltered hydrated-cement (Fig. 8), which is consistent with the Carey and Lichtner model and possibly the Blanc et al. model but not the Kulik and Kersten model. The X-ray CT image also shows a narrow zone of increased density at the boundary of the unaltered hydrated-cement (the dark blue band between the altered and unaltered regions), which is consistent with the narrow zone of decreased porosity shown in Figs. 5 & 6 for the Carey and Lichtner and Blanc et al. models.

Alternative Kinetic Models

Figure 9 compares the predicted mineralogical evolution for different assumptions on the rates for portlandite, amorphous silica, or C–S–H. The rates tested represent large deviations from the base case intended to capture the uncertainty represented by the range of rates considered in the literature. General observations emerge: first, changing the rates changes the mineralogical evolution; second, a net precipitation (i.e., an increase in volume of solids) is observed in the alteration zone for all scenarios considered.

This latter observation is emphasized in Figure 10 (note the change in *x*-axis range for Fig. 10). The second observation is, perhaps, the most significant, in that it demonstrates that net precipitation in the alteration zone is not impacted by uncertainties in the kinetics; this conclusion is particularly important in the context of self-sealing, as discussed below. The first observation, however, is also important, inasmuch as the alteration pattern predicted in the base case is consistent with the observations of Kutchko et al. (2007) whereas the other cases of extreme kinetics are inconsistent.

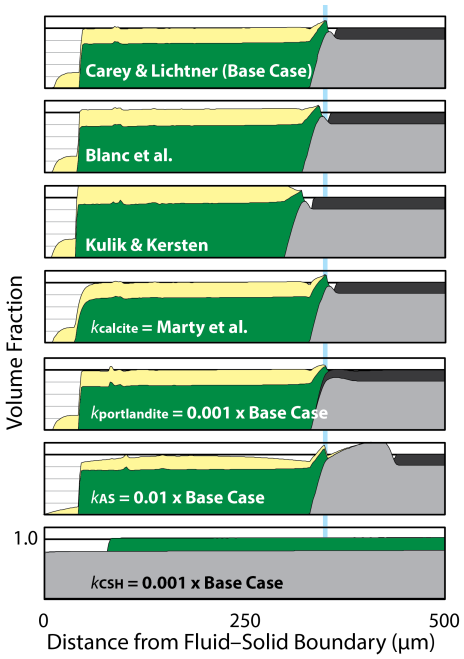

Figure 9. Simulations of the mineral alteration front for various thermodynamic and kinetic models. Top figure shows base case; remaining images show base case with different extremes of rates for calcite, portlandite, amorphous silica (AS), and C–S–H. Light blue line is shown as reference and is located at position of peak precipitation in the base case.

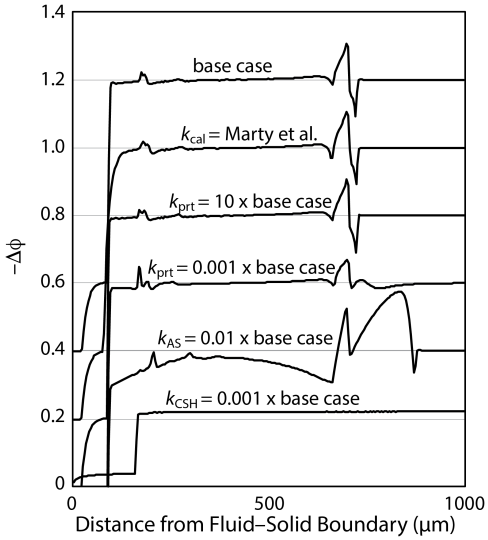

Figure 10. Simulated changes in porosity (shown as $-\Delta\phi$). Each graph is offset along the y-axis, with zero porosity change at 1.2 for the base case kinetics, 1.0 for low $k_{calcite}$, 0.8 for high $k_{portlandite}$, 0.6 for low $k_{portlandite}$, 0.4 for low k_{AS}, and 0.2 for low $k_{C–S–H}$.

Self-Sealing Case: Advective Alteration

We applied our thermodynamic and kinetic model to the case of advection-only alteration to probe an endmember scenario for self-sealing of a fracture. (Inclusion of a diffusion from the hydrated cement into the fracture would effectively add a source of reactants that would augment the observations below, so advection only is, essentially, a conservative scenario for self-sealing.)

These advection-only runs demonstrated:

- The thermodynamic and kinetic model we use predicts mineral alteration similar to that resulting from diffusive alteration of hydrated Portland cement by carbonated brine (as has been reported in other reactive-transport studies).
- All three thermodynamic models predict a narrow zone of net precipitation coincident with the region where self-sealing occurs; all three models predict this zone shifts as a function of Ca:Si ratio, occuring closer to the inlet of fluid (i.e., closer to the entry of a leakage pathway) and with a higher net precipitation for high calcium C–S–H.
- The predicted reaction zone is relatively consistent over the range in uncertainty in the kinetic models for calcite and portlandite. However, the lower ranges assessed for amorphous silica and C–S–H predict significantly different alteration patterns; the base-case rates for amorphous silica and C–S–H are more consistent with experimental and field observations inasmuch as they predict the formation of both amorphous silica and calcite as the sealing phases.
- The position of the self-sealing reaction zone moves along the wellbore in relation to fluid movement and fluid:cement ratio; the carbonated cement zone

Base Case (Carey & Lichtner C–S–H Model)

The base-case behavior was simulated for a system consistent with a fluid from an idealized limestone storage reservoir interacting with an idealized hydrated portland-cement: the inlet fluid was in equilibrium with 300-bar CO_2 and calcite, and the hydrated-cement consisted of 15% portlandite and 65% C–S–H (i.e., a fluid:solid ratio of 20:80) with a Ca:Si ratio of 1.5. Kinetics assumed base-case rates (shown as red in Fig. 4).

The time evolution of the reaction is shown in Figures 11–14. At 1 hour (Fig. 11), the reaction assemblage has already begun to develop, with a complete removal of portlandite, a partial removal of C–S–H, and a replacement by calcite and minor amount of amorphous silica. The reaction products already show a net volume increase over the reactants (i.e., porosity decreases). At 1 day (Fig. 12), the reaction front has progressed downstream from the fluid inlet, resulting in complete removal of C–S–H and additional precipitation of silica. As time progresses (Figs. 13 and 14), the reaction front continues to move downstream.

Two characteristics of the reaction emerge from this time sequence. First, the overall reaction replaces C–S–H and portlandite (which are stable in the hydrated-cement zone) with amorphous silica and calcite, which are stable with the carbonated brine over most of the region. This is illustrated by the regions of zero growth rate on either side of the reaction front, which is accompanied by regions of distinct but stable fluid chemistry (as seen by the constant pH, pCa, and pSi). The second characteristic is a narrow reaction zone separating these two regions. This "sealing-reaction zone" has a higher volume of solids than both the altered zone (calcite plus silica) and the unaltered zone (C–S–H plus portlandite), meaning that porosity is reduced (and sealing can occur).

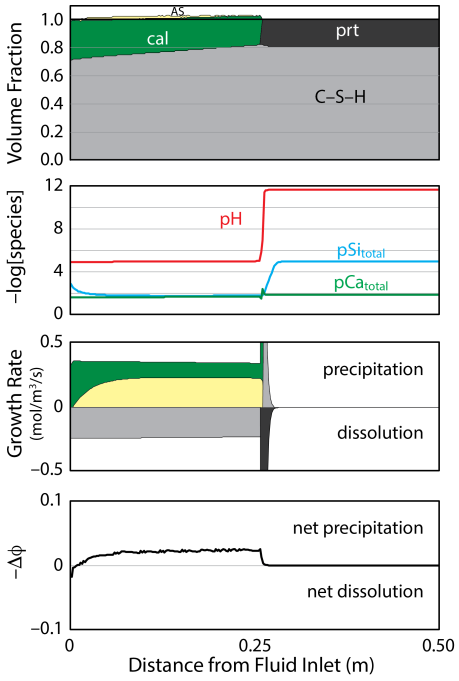

Figure 11. Simulated alteration after 1 hour of fluid flow for base-case scenario: 50 °C, 100 bar, limestone reservoir, Carey & Lichtner C–S–H with Ca:Si=1.5, base-case kinetics, and a fluid:solid ratio of 20:80 or 0.25.

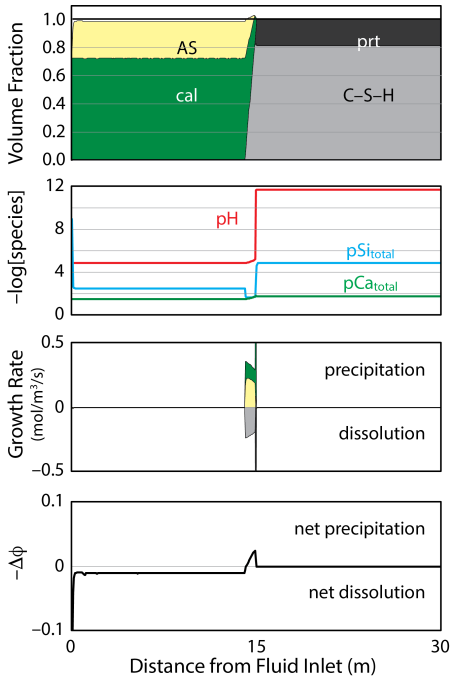

Figure 13. Simulated alteration after 1 week of fluid flow for scenario described in Fig. 11.

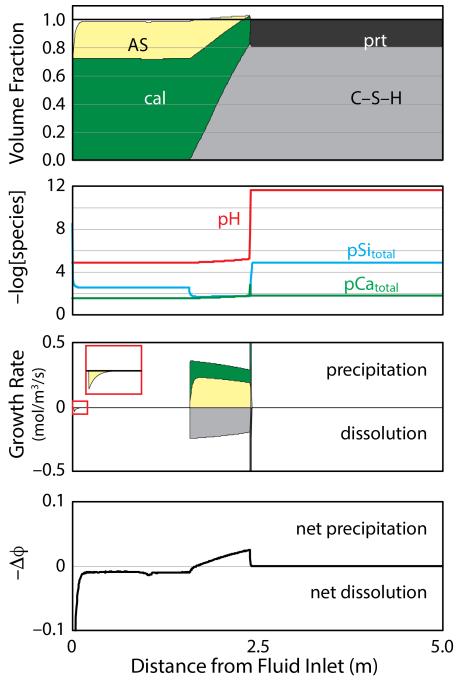

Figure 12. Simulated alteration after 1 day of fluid flow for scenario described in Fig. 11. Inset shows enlargement of area at fluid inlet designated by the red box.

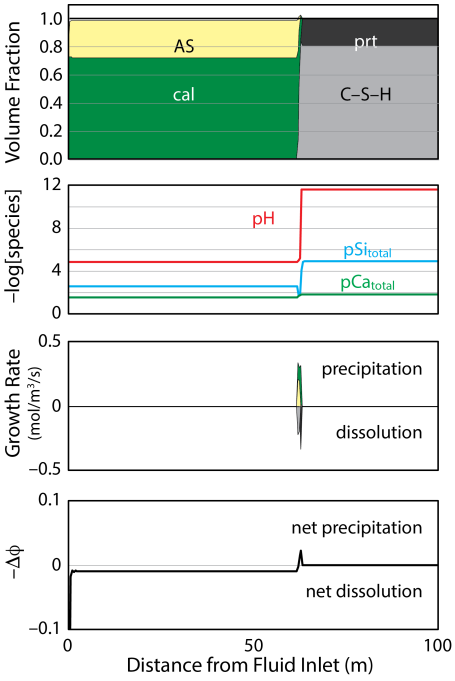

Figure 14. Simulated alteration after 1 month of fluid flow for scenario described in Fig. 11.

Geochemical Dynamics of Self-Sealing

Self-sealing requires precipitation. Hence, a critical insight into self-sealing is revealed through the evolution of dissolution and precipitation reactions in space and time, as illustrated by the graphs in Figures 11–14. Schematically, five geochemical zones can be derived from these simulations:

- *Zone I: Dissolution of solids by the incoming, under-saturated fluid.* Initially, this zone is entirely defined by dissolution of hydrated-cement phases (C–S–H and portlandite) (zone I-a), but eventually it includes a second zone where previously formed alteration phases (silica and carbonate) also dissolve (zone I-b). In a field-scale scenario, zone I is likely to occur only near the inlet of fluids flowing from the reservoir into the wellbore environment. In fact, it is sufficiently narrow as to be unresolved in Figures 13–14 due to the large grid spacing but it can be seen in the inset of Figure 12. (Note: Figure 12 assumed an input fluid from a limestone reservoir, so only silica is dissolving at the inlet.) As this zone involves dissolution, the flowpath can open (i.e., self-sealing cannot occur in this zone). The nature of this zone depends strongly on the chemistry of the fluids entering from the reservoir; for example, fluids equilibrated with a limestone reservoir will not dissolve any previously precipitated calcite.
- *Zone II: Equilibrium between fluid and solids.* Under most conditions, this zone is dominated by equilibrium with silica and carbonate, i.e., the early formed alteration products resulting from the carbonation of hydrated-cement. No net dissolution or precipitation occurs in zone II.
- *Zone III: Dissolution of C–S–H and precipitation of silica and carbonate.* This zone has a net increase in volume of solids, so it comprises part of the self-sealing reaction zone. Figs. 11–14 show net changes in volume assuming a dense amorphous silica, so they are conservative inasmuch as the silica precipitated in experimental systems is often described as a lower density material. Another attribute of this zone is an increase in dissolved silica (shown by the decrease in pSi), which becomes important in zone IV.
- *Zone IV: Dissolution of portlandite and precipitation of C–S–H and carbonate.* This zone has a net increase in volume of solids, so it also comprises part of the self-sealing reaction zone. It is noteworthy that this zone includes reaction of the previously released silica to form additional C–S–H.
- *Zone V: Equilibrium between fluid and solids.* In zone V, the fluids have reached equilibrium with the hydrated-cement phases.

These zones are similar to those observed in diffusion experiments (e.g., Kutchko et al., 2007 and as detailed above). However, advection collapses some zones into one. For example, in diffusion, zone IV has three distinct regions that separate calcite precipitation, C–S–H precipitation, and portlandite dissolution, resulting in a narrow band of increased porosity (Figs. 5–7), whereas in advection these three zones collapse in space and time. Nevertheless, the general patterns are very similar, with the self-sealing reaction zone (zones III and IV) reflecting the zone of dense precipitation observed in diffusion experiments (e.g., Fig. 8).

Hydrogeochemical Dynamics of Self-Sealing

To gain insight into where self-sealing can occur in space and time during advection, one must understand the migration of the sealing-reactions zones (zones III and IV) as a function of key parameters.

As noted above, several parameters can impact the evolution of the hydrogeochemical system (e.g., Ca:Si ratio, fluid composition, etc.), but two factors emerge as significant first-order drivers: fluid velocity and fluid:solid ratio.

A key characteristic of the dynamics of the self-sealing reaction zone is that its position along the wellbore moves proportional to fluid velocity and time. The proximity of the pH front to the

leading edge of the sealing-reaction zone offers a simple measure for tracking the position of the reaction front, and this is shown in Figure 15 for both early times in the development of the alteration and at later times when a new steady state is reached. For reference, the position of the fluid front is shown as a blue line. In both cases, the velocity of the reaction front is constant and a small fraction of the fluid velocity.

For a fluid:solid ratio of 0.25 (as shown in Fig. 15), the reaction front moves at ~20% of the velocity of the fluid front at early time points but slows to ~7% of the fluid-front velocity at later time points (Fig. 15). The system changes from one to the other over a period of ~2 hours to ~1 day, as a zone of fully altered hydrated-cement develops along the wellbore. Once this alteration zone develops, the self-sealing reaction zone moves at a relatively constant rate relative to the fluid out to at least a year (Fig. 16). Furthermore, these same ratios between fluid velocity and velocity of the reaction zone are found for different fluid velocities (note the constant displacement of circles below their corresponding lines in Fig. 16).

Based on these observations, the location of the self-sealing reaction zone (X_{SSRZ}) in space and time is proportional to the position of the fluid front; in other words, it is largely determined by:

$$X_{SSRZ}(t) = a(\text{f:s}) \times v_{fluid} \times \text{t} \qquad (4)$$

or

$$a(\text{f:s}) = \frac{X_{SSRZ}(t)}{X_{fluid}(t)} \qquad (5)$$

where:

- *a(f:s)* is the ratio of the distance traveled by the reaction front to the distance traveled by the fluid front or the ratio of the velocities of the fluid and reaction fronts at a given fluid:solid ratio (f:s).

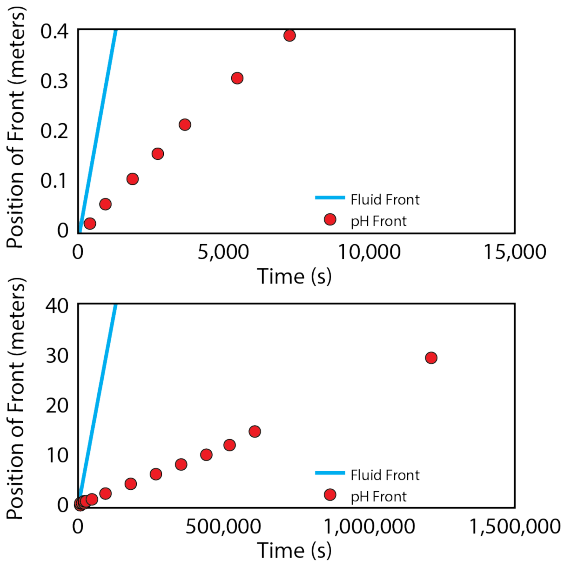

Figure 15. Plots of position of the sealing-reaction zone versus time as measured by the position of the pH front (circles); blue line shows the corresponding position of the fluid front. Top figure shows early stages of alteration, lower figure shows the steady-state of the sealing-reaction zone that develops after ~1 day. Calculations were for a fluid velocity of 10^4 m/yr (3.2×10^{-4} m/s) and a fluid:solid ratio of 0.25.

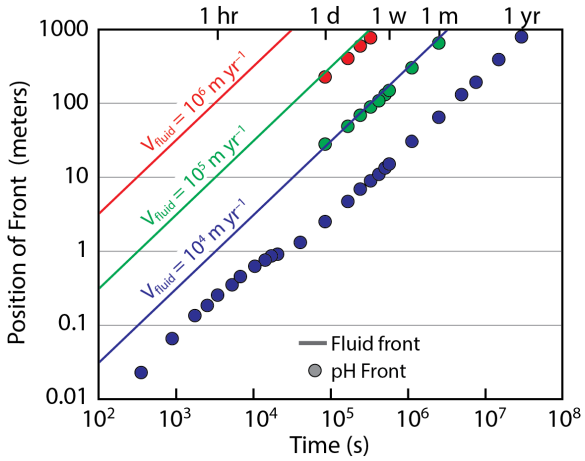

Figure 16. Position of the chemical and fluid fronts simulated for the base-case scenario: 50 °C, 100 bar, limestone reservoir, Carey & Lichtner C–S–H with Ca:Si=1.5, base-case kinetics, and a fluid:solid ratio of 0.25. Solid lines show fluid fronts, circles show reaction fronts.

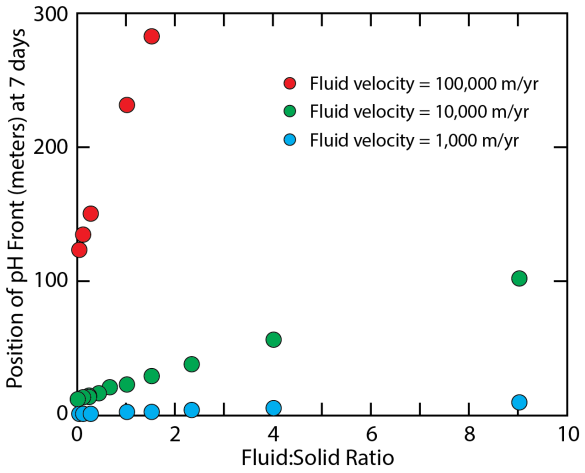

Figure 17. Variation in position of the pH front at 7 days as a function of fluid:solid ratio for three fluid velocities.

The dynamics of the self-sealing reaction are also a function of the volumetric fluid-to-solid ratio, where the volume of the solid is a measure of solid material that is accessible to the fluid—essentially a measure of the surface area associated with the roughness of the fracture and porosity of the hydrated-cement. Although our simulations did not allow for matrix–fracture interactions, these processes are important to consider in the context of fluid:solid ratio. Specifically, communication between the fracture fluid and matrix (e.g., via diffusion) provides another source term for reactants, effectively increasing the mass of solid (i.e., lowering the fluid:solid ratio). In other words, the matrix interactions can enhance the self-sealing dynamics.

Although the calculations above were done assuming a fluid:solid ratio of 20:80 (i.e., 0.25), several additional calculations were done varying this ratio, as shown in Figure 17.

As noted above, the time behavior of a(f:s) shows a long-term steady-state once the reaction zone has migrated past the inlet (less than 1 day for the conditions shown in Figure 16). In this steady-state condition, X_{SSRV} shows a linear relationship with the fluid-to-solid ratio (Fig. 17), implying that a(f:s) is also linear with the fluid:solid ratio (e.g., Eq. 5) at low fluid:solid ratios. Indeed, Figure 18 shows that a(f:s) is nearly linear in fluid-to-solid ratio, closely following the trend:

$$a(\text{f:s}) = 0.060 \times \frac{\text{V}_{\text{fluid}}}{\text{V}_{\text{solid}}} + 0.064 \qquad (6)$$

At high values of fluid:solid ratio, a(f:s) begins to deviate from the linear relationship as to be expected, given that a(f:s) must be less than or equal to 1 (i.e., the reaction front cannot travel faster than the fluid front). Hence, the fluid velocity provides an upper limit for the velocity of the reaction front at very high fluid:solid ratios.

Equation 6 implies a minimum value for the hypothetical condition of a fluid:solid ratio of zero; specifically, the reaction front moves at ~6% of the fluid front for a(0).

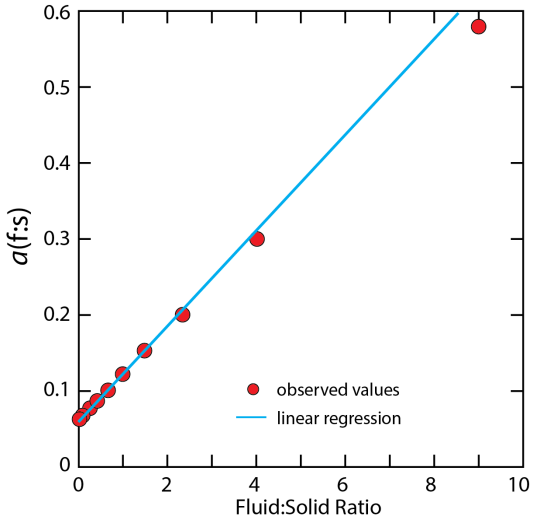

Figure 18. Variation in the position of the pH front at 7 days normalized to fluid velocity and time (i.e., 7 days). Red circles show the values observed in the simulations; blue line show a linear fit to the values for fluid:solid ratio less than 2, with the fit parameters given in Eq. 6.

Reaction Characteristics of Self Sealing

The analysis above is based on the position of the pH front, which is the leading edge of the self-sealing reaction front. However, one can gain a greater insight into the dynamics of the self-sealing reaction by considering how the entire

zone develops in relation to the fluid front—i.e., by normalizing distances to the position of the fluid front or the product of fluid velocity and time.

Figure 19 shows the characteristics of the self-sealing reaction zone plotted as a function of distance normalized to fluid velocity and time for $a(0)$. (In other words, although the graphs were calculated using a fluid:rock ratio of 0.25, the normalization adjusted the x-axis to a fluid:rock ratio of zero based on Eq. 6.) The analysis in Eq. 4 and Figs. 15–18 focused only on the position of the pH front relative to the fluid front, but Fig. 19 shows the positions of each part of the reaction zone relative to the position of the fluid front. The width over which this reaction sequence occurs is proportional to both fluid velocity and time, such that at higher fluid velocities and/or at longer times the sealing-reaction zone occurs over a larger area. In other words, the pH gradient moves at a faster rate (i.e., close to 0.064 on this plot or roughly 0.064 times as fast as the fluid) than the tail of the reaction (which is at about 0.059 on this plot).

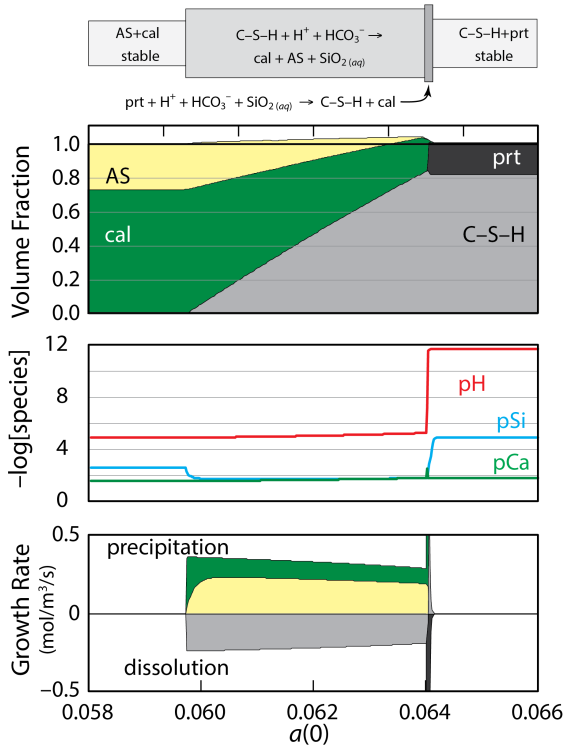

Figure 19. Details of the reaction sequence during reactive flow near the interface between hydrated Portland cement and carbonated C–S–H+portlandite. Horizontal units are in length normalized to fluid velocity and to time and assuming a fluid:solid ratio of 0 (i.e., $a(0)$ based on Eq. 5 and 6). Simulation assumed base-case conditions. Upper schematic shows reactions in each zone, with the box representing each zone qualitatively scaled to the relative volume of solids.

As noted above, the conversion of C–S–H and portlandite to amorphous silica and calcite occurs over a small region of dissolution and precipitation separating two regions of distinct fluid chemistry and their accompanying stable mineral assemblages. On one side of the self-sealing reaction zone, the fluid is in equilibrium with hydrated Portland cement (hPc), whereas on the other side the fluid is in equilibrium with carbonated hPc. Dissolution and precipitation rates are zero in each of these zones.

In the sealing-reaction zone, there is has a notable increase in the volume of solids, resulting in a decrease in porosity that can lead

to self-sealing. Indeed, self-sealing can only occur in a zone where precipitation is occurring, thus it can only occur in the narrow sealing-reaction zone (see Figs. 12–14) that contains both reactants (C–S–H and portlandite) and products (carbonate and silica). Self-sealing conditions do not, however, guarantee self-sealing will occur, which instead is a more complex function of precipitation rates and the volume of voids that must be sealed. Nevertheless, the sealing-reaction zone is a fundamental measure of where self-sealing can occur provided sufficient time is available for a specific sized void.

The sealing-reaction zone has two distinct regions (Fig. 19). The bulk of this zone is defined by the reaction of C–S–H with protons and bicarbonate to form calcite, amorphous silica, and aqueous silica. The pH increases slightly over this zone but still remains acidic. The second zone is defined by the reaction of portlandite with protons, aqueous CO_2, and aqueous silica (which has been transported from the C–S–H dissolution zone); the net result is a precipitation of calcite and C–S–H and a dramatic increase in pH. As noted, both of these zones have a higher volume of solids than the original material, and they coincide with the zone of self-sealing that has been observed experimentally and in the field.

It should be noted that our prediction of the precipitation of C–S–H in the second zone is likely a proxy for the precipitation of any of several possible calcium-silicate phases, driven by solubility changes at boundary where both pH and pCa change sharply. In a real system with an expanded set of chemical components, this could include calcium-aluminosilicate phases, etc. Indeed, Mason et al. (2013) report a zeolite-like phase—possibly mordenite or clinoptilolite based on local atomic structure—forming in the amorphous zones.

Variation in Predictions due to Uncertainty

As noted, there is significant uncertainty in both thermodynamic models for C–S–H and kinetic models for each of the phases. In this section, we assess the impact of this uncertainty on two parameters related to self-sealing: position of the reaction front (as measured by the steep pH gradient) and the intensity of self-sealing (as measured by the magnitude of the decrease in porosity).

Figure 20 shows the assessment of the thermodynamic uncertainty, both with respect to the three different models and with respect to the calcium to silicon ratio in the C–S–H. Two important observations can be made for all models shown. First, the reaction boundary occurs at a shorter distance from the inlet for higher Ca:Si ratios (e.g., compare Figs. 20a and 20h). Second, self-sealing (as reflected by a net reduction in porosity) is predicted to occur by all models. However, the intensity of the self-sealing (largest negative change in porosity) is strongest at higher Ca:Si ratios; in fact, for a Ca:Si ratio of 0.79, the Carey and Lichtner model predicts only a small degree of self-sealing at the reaction front and actually predicts an *increase* in porosity over much of the alteration zone (Fig. 20h $-\Delta\phi$ plot). Taken together, these two observations predict a stronger self-sealing behavior for high Ca:Si ratio C–S–H.

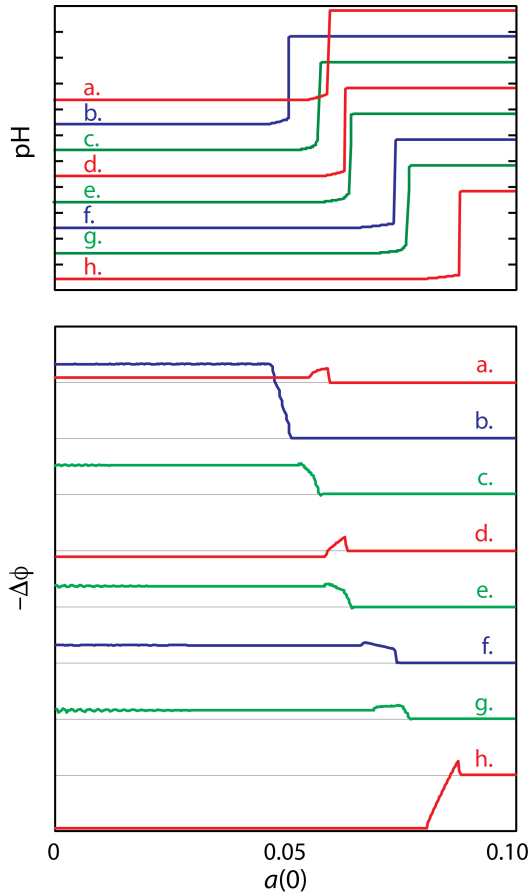

Figure 20. Variation in predicted reaction dynamics for the different thermodynamic models for C–S–H, normalized to fluid velocity and time and adjusted to a fluid:solid ratio of 0. Red curves correspond to the Carey & Lichtner models; blue curves correspond to the Kulik & Kersten models; green curves correspond to the Blanc et al. models. The letters indicate different Ca:Si ratios: a–1.70, b–1.67, c–1.60, d–1.50, e–1.20, f–0.83, g–0.80, h–0.79. The x-axis scale is normalized to fluid velocity and time. Tick marks for the pH graph correspond to 2 (i.e., a 10^2 variation in proton activity). For the plots of decrease in porosity, grid lines indicate a zero-porosity change for each plot. (Note: the saw-tooth pattern in the volume result from variation in calcite dissolution/precipitation as can be seen for example in Figs. 12–13. The frequency of the oscillations varies as a function of grid size, so it is likely an artifact.)

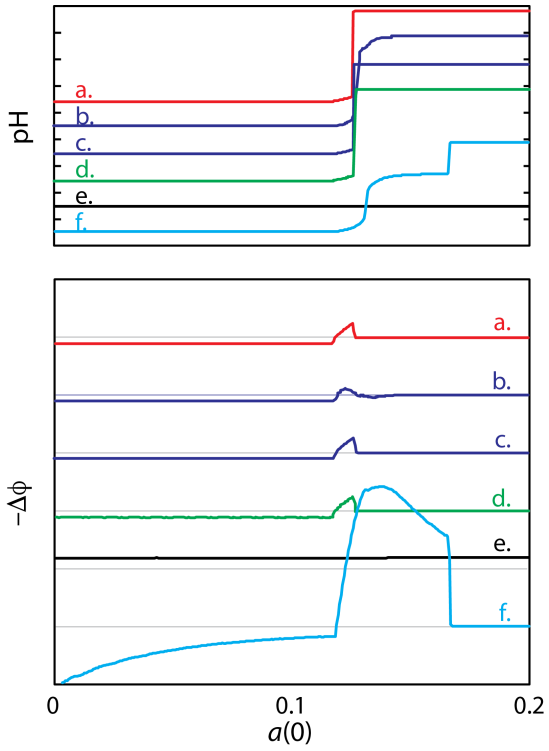

Figure 21. Variation in predicted reaction dynamics for the different kinetic models, all assuming the Carey & Lichtner C–S–H model with a Ca:Si ratio of 1.50. a) Base case; b) low portlandite rate; c) high portlandite rate; d) Marty et al. calcite model; e) low C–S–H rate; f) low amorphous silica rate. The x-axis scale is normalized to fluid velocity and time. Tick marks for the pH graph correspond to 2 (i.e., a 10^2 variation in proton activity). For the plots of decrease in porosity, grid lines indicate a zero-porosity change for each plot. Plots have been adjusted to a fluid:solid ratio of 0.

The uncertainty represented by the various thermodynamic models impacts both the prediction of reaction front and the intensity of the sealing. This former can be gauged by comparing the positions for a–b–c and f–g–h, as each grouping of the three models represents Ca:Si ratios that are close. At high Ca:Si, the thermodynamic models predict pH fronts that range from 5–6% of fluid velocity. At low Ca:Si, the thermodynamic models predict pH fronts that range from 7–9% of fluid velocity. Hence, with respect to the position of the reaction front relative to the fluid front, a range of 5–10% captures the uncertainty due to Ca:Si ratios and

the various thermodynamic models for a theoretical fluid:solid ratio of zero. With respect to the uncertainty in the intensity of self-sealing in the reaction front, the Kulik and Kersten models predict the highest reduction in porosity, whereas the Carey and Lichtner models predict the lowest.

Figure 21 shows the assessment of the kinetic uncertainty, using the Carey and Lichtner C–S–H model for a Ca:Si ratio of 1.50. In all cases, the models predict self-sealing will occur, albeit the low rate explored for portlandite (10^{-3} relative to the base case) predicts a relatively low intensity (Fig. 21b $-\Delta\phi$ plot). It should be noted that this low of a rate for portlandite was inconsistent with the experimental observations of Kutchko et al. (2007), so it may represent an overly conservative extreme. The assumption of a low rate for silica precipitation is particularly notable, in that it predicts an extreme reduction in porosity due to the re-precipitation of C–S–H; the re-precipitation of C–S–H has not been reported in experimental or field observations.

The predicted position of the reaction front is relatively insensitive to the variations in the reaction rate, with the exception of a very low rate for C–S–H (10^{-3} relative to the base case). In this latter case, the predicted position of the reaction front is displaced by a factor of >2x further downstream relative to the position predicted for the base case (Fig. 21e pH plot); nevertheless, this rate predicts an intense degree of sealing throughout the alteration zone. It should be noted that this low of a rate for C–S–H was inconsistent with the experimental observations of Kutchko et al. (2007), so this may represent an overly conservative extreme. The low rate explored for amorphous silica is also noteworthy: It predicts a very intense self-sealing response due to the transport of silica to the zone where pH begins to increase (dramatically increasing silica saturation and causing a large degree of precipitation).

In summary, the uncertainties and variabilities in the thermodynamic and kinetic models do not impact the general interpretations of self-sealing dynamics: the active reduction in porosity (i.e., self-sealing conditions) only occurs at the interface between carbonated and hydrated cement (i.e., where hydrated reactants are still present), and the position of this zone moves proportional to fluid velocity.

Discussion

Relevant Field Distances for Self-Sealing

Several key insights emerge from the analysis of the mechanisms and dynamics of self-sealing:

- *First, self-sealing only occurs in the self-sealing reaction zone, with relative stability on either side of the zone.* In other words, for a pathway to seal, part of the pathway must remain in the reaction zone long enough for precipitation to close the flowpath. The reaction only occurs when reactants—such as C–S–H and portlandite—are still in contact with the fluid. Once a section of wellbore is devoid of reactants (i.e., fully carbonated), it remains static chemically—so it neither opens nor closes.
- *Second, the sealing-reaction zone moves over time.* A slowly moving sealing-reaction zone is needed to maintain the zone in a region sufficiently long to allow for the sealing of a flowpath. The time needed to seal a pathway will, of course, vary, depending on the size of the pathway—in other words, a large volume pathway will require more time to fill.
- *Third, the velocity of the sealing-reaction zone is controlled by the velocity of the fluid, which in turn can be controlled by several factors.* The recognition that the velocity at which the sealing reaction moves is proportional to the velocity of the fluid provides a powerful insight into the conditions needed to maintain the sealing-reaction zone within a cemented region sufficiently long to allow the self-sealing process to close a flow path. Specifically, slow fluid velocities (limited by, for example, reservoir permeability and/or aperture size) result in a sufficiently slow migration of the reaction zone to promote sealing. However, the corollary to this observation is that fast fluid velocities will not favor self-sealing. For example, one can consider the relationships shown in Figure 16. For a fluid velocity of 10^4 m/yr ($3x10^{-4}$ m/s), the sealing-reaction zone will remain within a 10-meter section of cement for roughly a week, whereas a fluid moving at 10^6 m/yr ($3x10^{-2}$ m/s) will result in the sealing-reaction zone remaining within a 10-meter for less than an hour. In other words, fast moving fluids may not allow for sufficient time for a flow pathway to be sealed.

One implication is that slow fluid velocities promote self-sealing. In this section, we explore some of the conditions that can limit fluid velocity:

- A small aperture for fracture flow;
- Maintaining a low driving pressure between the storage reservoir and the reservoir into which the fluid flows, such as may occur during early stages of an injection or as a result of active reservoir management practices;

Two other cases include:

- Low permeability for porous flow, where the limiting permeability can occur in the storage reservoir or in a cemented section of wellbore on either side of an open flowpath;
- Drag associated with the boundary characteristics of an open channel flow in the wellbore.

This latter scenario is equivalent to an open wellbore and does not provide sufficient drag to limit flow to enable self-sealing conditions; so, it is not assessed in detail here. Although the former scenario is not assessed in detail here, it can be an important factor in promoting wellbore integrity: for example, by ensuring that at least some of the wellbore is completely cemented, flow on any open pathway elsewhere in the wellbore will be limited such that self-sealing will be promoted.

Aperture-Limited Flow

As an approximation to aperture-limited flow on a fracture, we consider apertures with transport properties that are consistent with the cubic-

rate law, which can be cast as an average velocity ($\vec{v}$) as:

$$\vec{v}\ \left(\frac{m}{s}\right) = -\,|\nabla P|\ h^2\ (12\ \mu)^{-1} \qquad (7)$$

(e.g., Zimmerman and Bodvarsson, 1994) where:

- ∇P is the pressure gradient defined by the change in pressure (in pascals) over a specific distance (in meters);
- *h* is the hydraulic aperture (in meters); and
- μ is the viscosity of the fluid (in pascal-seconds)

Using this relationship, one can calculate the predicted position of the sealing-reaction front using Eq. 6, assuming the velocity is aperture limited and assuming a conservative estimate for the linear rate of calcite precipitation based on data in Table 3. This latter assumption allows the aperture size to change dynamically as calcite precipitates. At 50°C, the linear precipitation rate for calcite assuming the neutral-mechanism rate given in Table 3 and based on the geometric surface area of the fracture is roughly 10 μm d^{-1} (based on a rate of $10^{-5.49}$ mol/m^2/s and a molar volume of 36.934 cm^3/mol), resulting in a dynamic change in the aperture given by:

$$h(\mu m) = h_0(\mu m) - 0.000116(\mu m\ s^{-1}) \times t(s) \qquad (8)$$

where h_0 is the initial fracture aperture. Figures 22–24 show such plots for an initial aperture of 10-μm, 50-μm, and 100-μm with the base-case parameters and for various overpressures in the storage reservoir. The upper bounds represent the evolution of the fluid front, whereas the lower bounds represent the hypothetical endmember for a fluid:solid ratio of 0. Two conclusions emerge from these plots:

- *Small fractures (e.g., <10-μm) should maintain sufficiently slow velocities to enable self-sealing, even assuming high fluid:solid ratios.* In fact, 10-μm fractures should self-seal within 10s of meters and likely much less (i.e., within meters), and they should self-seal relatively rapidly (on the order of a day).
- *Large fractures, however, may not maintain sufficiently slow velocities to enable self-sealing, if the velocity is aperture limited.* In the examples analyzed, 50-μm fractures may self-seal if low overpressures are maintained (i.e., in the case of active-reservoir management), but fractures on the order of 100 μm and greater will not limit flow sufficiently well to ensure self-sealing in less than 100s of meters in the absence of other limitations to flow (such as reservoir permeability and/or porous flow conditions in the well either above or below the fracture).

One uncertainty in this analysis is the time required to seal a fracture of a given size. Predicting this time is challenging, because (1) it is coupled with fluid velocity and (2) it relies on several poorly constrained factors, principally precipitation rate and surface area. The second of these is highly variable, depending on roughness of the fracture, the size and number of nucleated crystals, the frequency of key defects (such as screw dislocations in calcite, which can serve as sites of rapid crystallization via spiral growth), and fluid chemistry (which can inhibit or accelerate precipitation). As noted, we assumed a very conservative surface area (geometric surface area of the fracture), so our conclusion of a rapid filling of fractures up to 10 μm by calcite over short distances (see Fig. 22) is also conservative. We focused on calcite precipitation, because it is significantly faster than that for silica. Finally, this analysis does not imply that larger fractures will not also seal; rather, realistic precipitation rates and reservoir-limited flow are likely to favor sealing conditions for even much larger fractures.

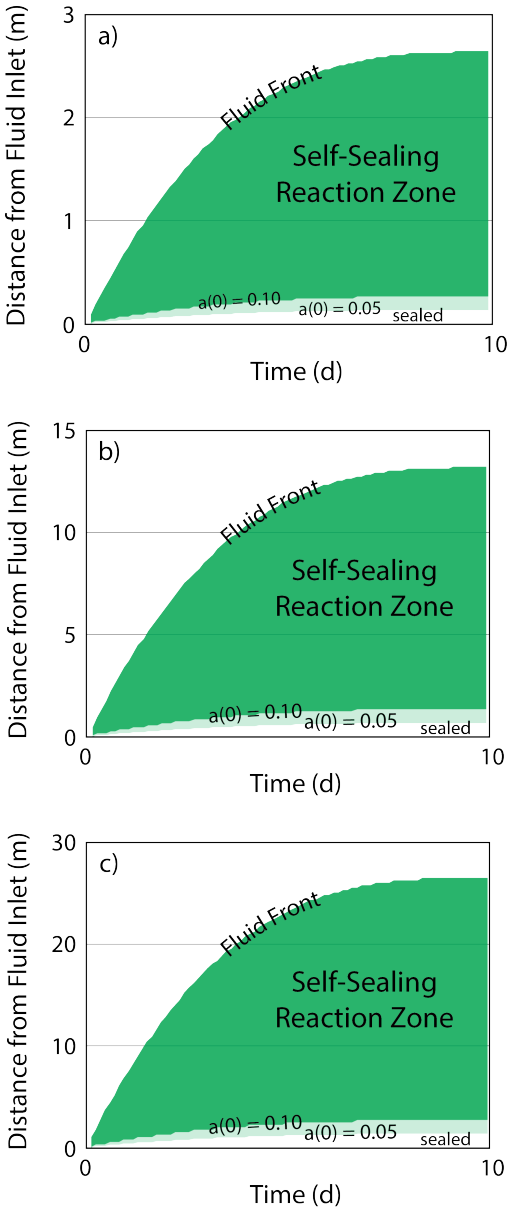

Figure 22. Sealing-reaction zone for a 10-µm fracture assuming that fluid velocity is controlled by a cubic-law aperture and assuming that calcite precipitates from time t=0 consistent with Eq. 6. Images show overpressures relative to hydrostatic of (a) 1 MPa, (b) 5 MPa, (c) 10 MPa. Water viscosity was assumed to be 0.89 mPa-s. Upper bound is for high fluid:solid ratios (reaction front is coincident with fluid front), whereas lower bounds are for a fluid:solid ratio of 0—i.e., $a(0)$. The two values for $a(0)$ bracket the range shown for C–S–H uncertainty as reflected in Fig. 20.

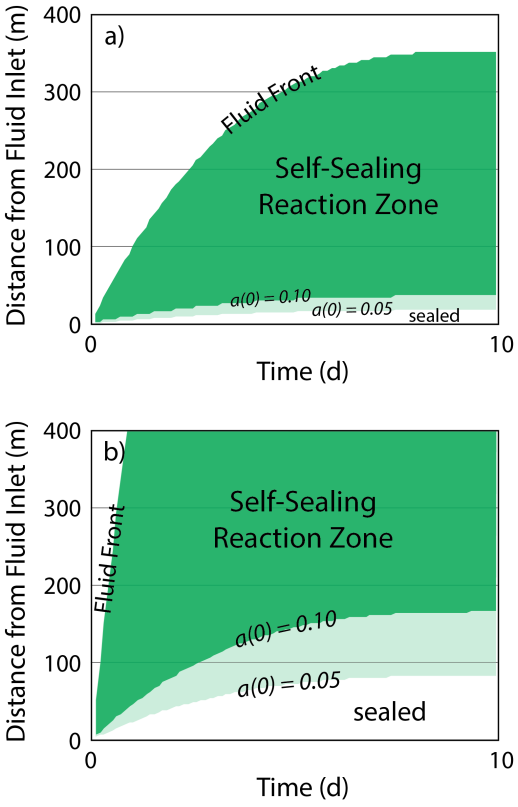

Figure 23. Sealing-reaction zone for a 50-µm fracture assuming that fluid velocity is controlled by a cubic-law aperture (see details in Fig. 22). Images show overpressures relative to hydrostatic of (a) 1 MPa, (b) 5 MPa.

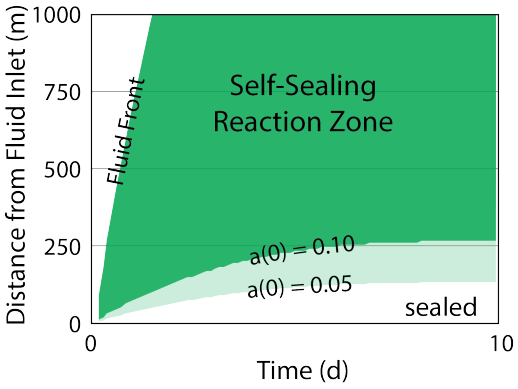

Figure 24. Sealing-reaction zone for a 100-µm fracture assuming that fluid velocity is controlled by a cubic-law aperture (see details in Fig. 22). Image shows an overpressure relative to hydrostatic of 1 MPa.

Pressure-Limited Flow

A perhaps obvious result from the scenarios investigated above is that management of reservoir pressure can minimize the drive for any leakage pathway, thereby limiting fluid velocities and promoting self-sealing.

For example, a comparison of Figs. 22a–c shows that for a given aperture size self-sealing is maintained closer to the fluid inlet for lower overpressures. Indeed, at an overpressure of 0, the pressure contributions to the driving force are eliminated.

Hence, active reservoir management strategies (e.g., co-production of connate fluids) can be used to maintain conditions that promote self-sealing.

However, other factors can also limit the over pressure in the reservoir. Here we explore pressure evolution during early stages of the injection and the implications on dynamics of the self-sealing reaction zone.

Figure 25 shows how pressure evolution during injection impacts fluid velocity in leaking well. In this example, the leaking well—which is offset by 1 kilometer from the injection well—experiences different fluid velocities for reservoirs of different permeabilities. Specifically, a high permeability reservoir maintains a low fluid velocity in the leaking well for over half a year before increasing, whereas a low permeability reservoir experiences rising fluid velocities early in the injection. This behavior ties to pressure evolution in the reservoir, and it is opposite of the behavior expected for fluid velocities at a constant pressure (as might occur during the post-closure phase). In this latter case, steady-state fluid velocities will ultimately be limited by reservoir permeability such that lower permeability results in lower fluid velocities.

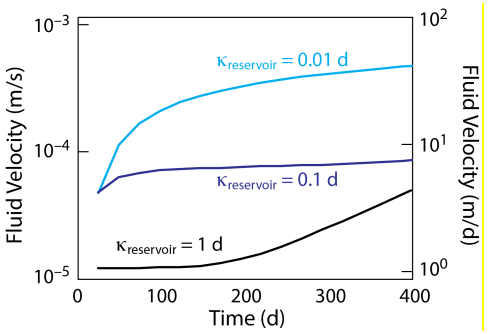

Figure 25. Simulation of fluid velocity in a wellbore assuming coupled flow from a reservoir (with three different permeabilities) into and along a wellbore with an effective permeability of 100 d during the early stages of a 1 $MtCO_2$ per year operation injected at 1-km depth. Leaking wellbore is displaced 1-km from the injection well. The abscissa shows time since initiation of injection.

The fluid velocities in Fig. 25 can be used to bracket the spatial evolution of the self-sealing zone, using data in Figs. 18 and 20. Figure 26 shows the spatial evolution of the self-sealing reaction zone over time for the three reservoir permeabilities. A high permeability reservoir (e.g., 1 d) will maintain the reaction front to within 50 m of the inlet for at least a couple months for high fluid:solid ratios and for over a year for low fluid:solid ratios. However, the reaction zone migrates rapidly for a 0.01-d reservoir at high fluid:solid ratios. In this latter case, if self-sealing does not occur rapidly, it is unlikely to occur.

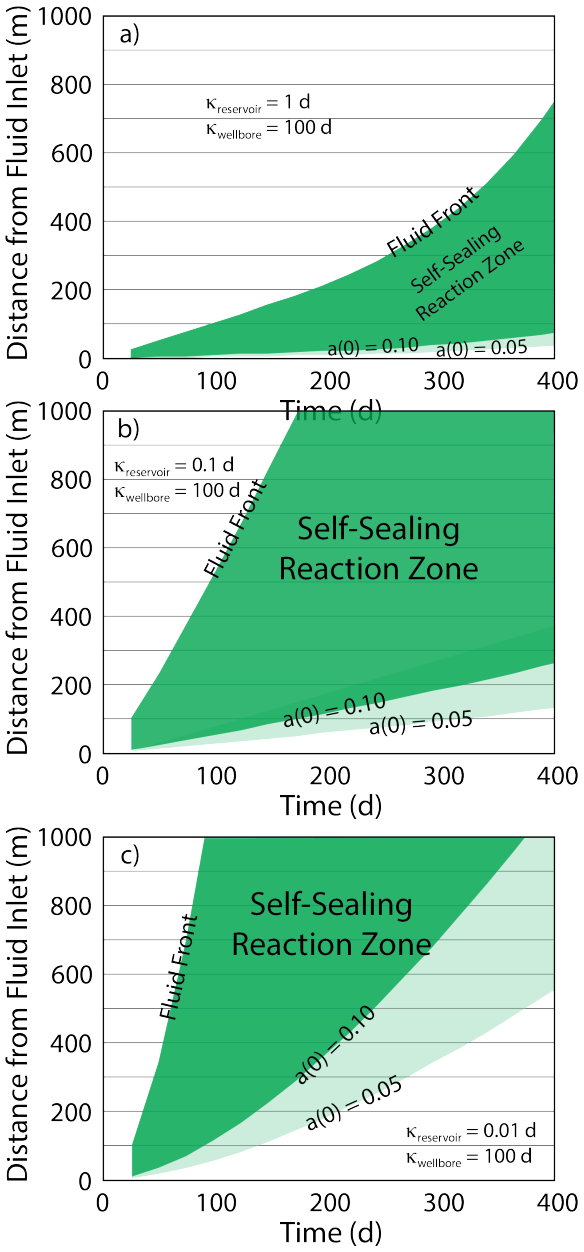

Figure 26. Predicted position of the chemical reaction front as a function of time assuming the fluid velocities shown in Fig. 25. Boundaries correspond to those defined in Fig. 22. a) Reservoir permeability is 1 d; b) Reservoir permeability is 0.1 d; c) Reservoir permeability is 0.01 d.

Lab versus Field

Different Mechanisms

Scaling from laboratory observations to field predictions is a widely recognized challenge in studies of natural systems: Do laboratory studies shed light on field-scale behavior, and, if so, how can the results be scaled appropriately?

Often, the approach to this question focuses on the differences in length and time scales, and the conceptual framework we present suggests that these differences in scale are particularly significant in the context of self-sealing. Given the difference in both length and time scales, laboratory and field behavior are likely governed by different mechanisms albeit tied to the same phenomena. In particular, there are at least two endmember cases that apply:

- *Small length and time scales of lab samples result in a model system that captures only part of the process at any one time.* For example, consider Figs. 11–14, which show the evolution of the system as a function of length and time for a specific flow rate. A laboratory sample of a few tens of centimeters would capture only a small slice of any of these figures, i.e., a small section of the wellbore dynamics in space and time. However, the dynamic evolution of each zone in the overall wellbore system depends on capturing processes across space and time: what happens in one zone affects what happens in the next zone in the flow path. For example, the reaction with portlandite at field scale requires that the fluid has already been precipitating calcite and silica and dissolving C–S–H, otherwise the chemistry will not reproduce the appropriate mineralogical mechanisms (e.g., Fig. 19). In a lab experiment, the samples and timescales are too short to allow the development of the full sequence of geochemical environments that occur in the field. Hence, scaling from a lab experiment to a field parameter (such as permeability evolution) requires a

consideration of the larger time and space scales.

- *Different acidic fluids produce different self-sealing mechanisms.* The self-sealing process has generally been considered to result from a simple acid-base reaction, leading some studies to focus on pH as the sole fluid factor. However, the reaction sequences shown in Fig. 19 are more complex and involve dissolution and precipitation reactions with several minerals and several aqueous species. Although experiments utilizing different fluid chemistries—such as the hydrochloric acid experiments of Huerta et al. (2013)—can produce self-sealing, the geochemical mechanisms will differ from what would occur in the field.

These observations are not meant to imply lab-scale experiments provide no insight into field-scale behavior. Indeed, lab scale experiments are critical in elucidating the complex coupled processes that occur in a field scenario. Rather, the observations are meant to underscore the importance of coupling lab-scale experiments with appropriate simulations to capture the dynamics that occur at larger scales.

Residence Time versus Fluid Velocity

Several recent experimental studies have emphasized residence time of the fluid as a critical parameter to define conditions conducive to self-sealing (e.g., Brunet et al., 2016; Wolterbeek et al., 2016). Indeed, residence time is a critical parameter for the length and time scales relevant to experiment systems: a fluid must have sufficient time to interact with the wellbore materials so that the fluid's composition can evolve appropriately.

However, in a field-scale scenario, residence time is only relevant at very early stages in the development of the self-sealing process, either in the first few hours (Fig. 16) and/or right at the point of entry where fluids enter the wellbore from the reservoir. Under these conditions, the mechanisms differ from those that develop once the system reaches steady state and self-sealing reactions operate.

The velocity of the reaction front relative to the fluid front provides a more appropriate measure to assess self-sealing conditions in the field. While it embodies residence time, it allows the incorporation of other factors relevant at the field scale, particularly when it is coupled with the reactive transport phenomena outlined above. Furthermore, it can provide a link between reaction dynamics and a field-measurable parameter (leakage velocities) thereby enabling an assessment of when and where sealing conditions are likely to occur.

What happens in a real fracture?

As noted above, our analysis focused on quantifying specific, isolated relationships, so we assumed constant fluid velocity. However, in a real fracture, fluid flow and reaction-induced changes in permeability are coupled, and these coupled effects would have to be accounted for to simulate the details of self-sealing in a specific fracture.

Furthermore, most scenarios involving fracture flow are likely to exhibit variable fluid flow conditions along the fracture, irrespective of any coupled feedback between flow and reaction. Initially, these variations in flow may tie to variations in aperture both longitudinally and laterally along a fracture; however, as self-sealing reactions proceed, flow may become channeled within a fracture—as has been observed experimentally (Huerta et al., 2013).

Finally, dynamic geomechanical response of the system represents an additional factor that can alter fluid flow (Walsh et al., 2014). Carroll et al. (2017), present a coupled chemical and mechanical analysis of self-sealing, considering the scenario of the impact of diffusive alteration on mechanical properties of the alteration zone, which can lead to stress-induced closing of the fracture.

In order to capture the exact behavior of self-sealing for a specific flow scenario, one must consider the impact of each of these processes. By focusing on the isolated analysis of advective alteration, our intent was to quantify the impact of that process specifically. As noted, omitting these other processes does not invalidate our analysis; rather it is analogous to evaluating a partial derivative (e.g., holding geomechanical conditions or permeability constant). Including these processes, particularly geomechanics, enhances self-sealing such that our analysis is likely to be conservative.

Fluid:Solid Ratio

The fluid:solid ratio is a concept easily quantified geochemically but perhaps difficult to characterize in a field scenario. In essence, this parameter is a measure of how much solid material along a pathway is interacting with the flowing fluid.

In general terms, rough, small fractures are likely to have a low fluid:solid ratio, whereas smooth, large fractures are likely to have a higher fluid:solid ratio. Moving to more specific or quantitative field insights, however, will require further investigation. Nevertheless, the general insights raise intriguing questions. For example, might foamed cements lead to fractures with higher surface areas and, hence, more favorable fluid:solid ratios? Or, do strategies that lower the porosity of hydrated-cement in order to make it "more resistant" actually work counter to the material's innate self-sealing attributes? (This latter becomes even more intriguing given that many of these strategies to lower porosity also lower the Ca:Si ratio, which dampens the self-sealing properties of the hydrated cement.)

Additional research will be needed to elucidate quantitative fluid:solid ratios for various scenarios observed in the field.

C–S–H and Portlandite as a Carbonic Cement

In addition to shedding light on self-sealing, the reactions explored above reveal an important attribute of hydrated Portland cement. Specifically, it qualifies as a *carbonic cement* and therefore CO_2 resistant.

Since the Romans (and perhaps even earlier), Portland-based cement has been widely recognized as a hydraulic cement, meaning that it is a material that sets in the presence of water and maintains its integrity in the presence of water. By design, Portland cements—which consist of a mixture of several minerals, including Ca_3SiO_5 and Ca_2SiO_4—react readily with water, dissolving rapidly and causing the precipitation the reaction products that constitute hydrated Portland cement—a suite of hydrated phases, including C–S–H and portlandite, that are stable in water.

By extension, hydrated Portland cement is a carbonic cement in that it reacts with and sets in the presence of carbonic acid, and the resulting phases (silica and calcium carbonate) are stable in the presence of carbonic acid. Indeed, the silica and calcite are ubiquitous as "cements" in natural environments, where they are known to have sealed flow pathways (such as fractures) for geologic times.

Perhaps paradoxically, a "CO_2-resistant" cement may in fact include cements that react with CO_2 to produce an end product that is resistant. The use of carbonic acid to activate a cementitious material has been explored in some structural applications (e.g., Das et al., 2014), where slag is used as an admixture to produce iron carbonate. However, the recognition that C–S–H and portlandite (i.e., the main components in hydrated Portland cement) can be activated by carbonic acid to produce a CO_2 resistant end product could have profound implications for strategies to ensure wellbore integrity in CO_2 rich brine environments.

Acknowledgements

This work was funded by the US DOE's Office of Fossil Energy through its Carbon Storage Program as managed by the National Energy Technology Laboratory's Strategic Center for Coal. We would specifically like to thank Traci Rodosta and Josh Hull for their support and guidance throughout the course of this work. We would also like to thank Dr. Barbara Kutchko for many helpful discussions on the nature of hydrated-cement alteration. Los Alamos National Laboratory, an affirmative action/equal opportunity employer, is operated by Los Alamos National Security, LLC, for the National Nuclear Security Administration of the U.S. Department of Energy under contract DE-AC52-06NA25396.

References

Abdoulghafour, H., Luquot, L., Gouze, P. (2013) Characterization of the mechanisms controlling the permeability changes of fractured cements flowed through by CO_2 rich brine. *Environmental Science & Technology* **47:** 10332–10338.

Abdoulghafour, H., P. Gouze, L. Luquot and R. Leprovosta (2016). Characterization and modeling of the alteration of fractured class-G Portland cement during flow of CO_2-rich brine. *International Journal of Greenhouse Gas Control*.

Barlet-Gouédard, V., G. Rimmelé, O. Porcherie, N. Quisel and J. Desroches (2009). A solution against well cement degradation under CO_2 geological storage environment. *International Journal of Greenhouse Gas Control* **3:** 206–216.

Blanc, P., X. Bourbon, A. Lassin and E. C. Gaucher (2010). Chemical model for cement-based materials: Temperature dependence of thermodynamic functions for nanocrystalline and crystalline C–S–H phases. *Cement and Concrete Research* **40:** 851–866.

Blanc, P., A. Lassin, P. Piantone, M. Azaroual, N. Jacquemet, A. Fabbri and E. C. Gaucher (2012). Thermoddem: A geochemical database focused on low temperature water/rock interactions and waste materials. *Applied Geochemistry* **27:** 2107–2116.

Brunet, J.-P. L., L. Li, Z. T. Karpyn, B. G. Kutchko, B. Strazisar and G. Bromhal (2013). Dynamic evolution of cement composition and transport properties under conditions relevant to geological carbon sequestration. *Energy and Fuels* **27:** 4208–4220.

Brunet, J.-P. L., L. Li, Z. T. Karpyn and N. J. Huerta (2016). Fracture opening or self-sealing: Critical residence time as a unifying parameter for cement–CO_2–brine interactions. *International Journal of Greenhouse Gas Control* **47:** 25–37.

Carey, J.W. (2013). Geochemistry of wellbore integrity in CO_2 sequestration: Portland cement–steel–brine–CO_2 interactions. In: DePaolo, D.J., Cole, D.,Navrotsky, A., Bourg, I. (Eds.), *Geochemistry of Geologic CO_2 Sequestration: Reviews in Mineralogy and Geochemistry.* Mineralogical Society of America, Washington, DC, pp. 505–539.

Carey, J. W. and Lichtner, P. C. (2007). Calcium silicate hydrate (C–S–H) solid solution model applied to cement degradation using the continuum reactive transport model FLOTRAN. *Transport Properties and Concrete Quality: Materials Science of Concrete*. B. Mobasher and J. Skalny. Hoboken, New Jersey, John Wiley & Sons: 73–106.

Carey, J.W., Lichtner, P.C. (2011). Computational studies of two-phase cement–CO_2–brine interaction in wellbore environment. *SPE Journal*. **16:**940–948.

Carey, J. W.; Svec, R.; Grigg, R.; Zhang, J.; Crow, W. (2010) Experimental investigation of wellbore integrity and CO_2-brine flow along the casing-cement microannulus. *International Journal of Greenhouse Gas Control* **4:**272−282.

Carey, J. W., M. Wigand, S. J. Chipera, G. WoldeGabriel, R. Pawar, P. C. Lichtner, S. C. Wehner, M. A. Raines and G. D. Guthrie, Jr. (2007). Analysis and performance of oil well cement with

30 years of CO_2 exposure from the SACROC Unit, West Texas, USA. *International Journal of Greenhouse Gas Control* **1:** 75–85.

Carroll, S., J. W. Carey, D. Dzombak, N. J. Huerta, L. Li, T. Richard, W. Um, S. D. C. Walsh and L. Zhang (2016). Review: Role of chemistry, mechanics, and transport on well integrity in CO_2 storage environments. *International Journal of Greenhouse Gas Control* **49:** 149–160.

Carroll, S. A., W. W. McNab and S. Torres (2011). Experimental study of cement–sandstone/shale–brine–CO_2 interactions. *Geochemical Transactions* **12:** 9–27.

Carroll, S. A., Iyer, J., and Walsh. S. D. C. (2017) Influence of chemical, mechanical, and transport processes on wellbore leakage from geologic CO_2 storage reservoirs. *Accounts of Chemical Research* (http://pubs.acs.org/doi/abs/10.1021/acs.accounts.7b00094).

Crow, W., Williams, B., Carey, J.W., Celia, M., Gasda, S. (2009). Wellbore integrity analysis of a natural CO2 producer. *Energy Procedia: 9th International Conference on Greenhouse Gas Control Technologies*, **1:**3561–3569.

Crow, W.; Carey, J. W.; Gasda, S.; Williams, D. B.; Celia, M. (2010). Wellbore integrity analysis of a natural CO_2 producer. *International Journal of Greenhouse Gas Control* **4:**186−197.

Das, S., Souliman, B., Stone, D., and Neithalath, N. (2014) Synthesis and properties of a novel structural binder utilizing the chemistry of iron carbonation. *ACS Applied Materials & Interfaces*, 6:8295–8304.

Duan, Z. and R. Sun (2003). An improved model calculating CO_2 solubility in pure water and aqueous NaCl solutions from 273 to 533 K and from 0 to 2000 bar. *Chemical Geology* **193:** 257–271.

Duguid, A., M. Radonjic and G. W. Scherer (2011). Degradation of cement at the reservoir/cement interface from exposure to carbonated brine. *International Journal of Greenhouse Gas Control* **5:** 1413–1428.

Duguid, A. and G. W. Scherer (2010). Degradation of oilwell cement due to exposure to carbonated brine. *International Journal of Greenhouse Gas Control* **4:** 546–560.

Gasda, S. E., S. Bachu and M. A. Celia (2004). Spatial characterization of the location of potentially leaky wells penetrating a deep saline aquifer in a mature sedimentary basin. *Environmental Geology* **46:** 707–720.

Greenberg, S. A. and T. N. Chang (1965). Investigation of the colloidal hydrated calcium silicates. II. Solubility relationships in the calcium oxide-silica-water system at 25°. *Journal of Physical Chemistry* **69(1):** 182–188.

Guthrie, G. D., Jr. and J. W. Carey (2015). A thermodynamic and kinetic model for paste–aggregate interactions and the alkali–silica reaction. *Cement and Concrete Composites* **76:** 107–120.

Hammond, G. E., P. C. Lichtner, C. Lu and R. T. Mills (2012). PFLOTRAN: Reactive flow and transport code for use on laptops to leadership-class supercomputers. *Groundwater*

Reactive Transport Models. F. Zhang, G. T. Yeh and J. C. Parker. Sharjah, UAE, Bentham Science Publishers: 141–159.

Harp, D. R.; Pawar, R.; Gable, C. W. (2014) Numerical Modeling of Cemented Wellbore Leakage from Storage Reservoirs with Secondary Capture due to Thief Zones. *Energy Procedia* **63:**3532–3543.

Harp, D. R.; Pawar, R.; Carey, J. W.; Gable, C. W. (2016) Reduced Order Models of Transient Wellbore Leakage at Geologic Carbon Sequestration Sites. *International Journal of Greenhouse Gas Control* **45:**150–162.

Huerta, N. J., S. L. Bryant, B. R. Strazisar and M. Hesse (2011). Dynamic alteration along a fractured cement/cement interface: Implications for long term leakage risk along a well with an annulus defect. *Energy Procedia* **4:** 5398–5405.

Huerta, N. J., M. A. Hesse, S. L. Bryant, B. R. Strazisar and C. Lopano (2016). Reactive transport of CO_2-saturated water in a cement fracture: Application to wellbore leakage during geologic CO_2 storage. *International Journal of Greenhouse Gas Control* **44:** 276–289.

Huerta, N. J., Q. C. Wenning, M. A. Hesse, S. L. Bryant, C. L. Lopano and B. R. Strazisar (2013). Development of reacted channel during flow of CO_2 rich water along a cement fracture. *Energy Procedia* **37:** 5692–5701.

Huet, B., V. Tasoti and I. Khalfallah (2011). A review of Portland cement carbonation mechanisms in CO2 rich environment. *Energy Procedia* **4:** 5275–5282.

Jordan, A. B., Stauffer, P. H., Harp, D., Carey, J. W., Pawar, R. J. (2015). A response surface model to predict CO_2 and brine leakage along cemented wellbores. *International Journal of Greenhouse Gas Control* **33:**27–39.

Kulik, D. A. and M. Kersten (2001). Aqueous solubility diagrams for cementitious waste stabilization systems: II, End-member stoichiometries of ideal calcium silicates hydrate solid solutions. *Journal of the American Ceramic Society* **84(12):** 3017–3026.

Kutchko, B. G., B. R. Strazisar, D. A. Dzombak, G. V. Lowry and N. Thaulow (2007). Degradation of well cement by CO_2 under geologic sequestration conditions. *Environmental Science & Technology* **41:** 4787–4792.

Kutchko, B. G., B. R. Strazisar, S. B. Hawthorne, C. L. Lopano, D. J. Miller, J. A. Hakala and G. D. Guthrie (2011). H_2S–CO_2 reaction with hydrated Class H well cement: Acid-gas injection and CO2 co-sequestration. *International Journal of Greenhouse Gas Control* **5:** 880–888.

Kutchko, B. G., B. R. Strazisar, N. Huerta, G. V. Lowry, D. A. Dzombak and N. Thaulow (2009). CO_2 Reaction with Hydrated Class H well cement under geologic sequestration conditions: Effects of flyash admixtures. *Environmental Science & Technology* **43:** 3947–3952.

Lichtner, P. C., G. E. Hammond, C. Lu, S. Karra, G. Bisht, B. Andre, R. Mills, J. Kumar and J. M. Frederick (2017). PFLOTRAN Documentation Release 1.1. pflotran.org: 560.

Lichtner, P. C., G. E. Hammond, C. Lu, S. Karra, G. Bisht, B. Andre, R. T. Mills and J. Kumar. (2014). "PFLOTRAN User Manual: A massively parallel reactive flow and transport model for

describing surface and subsurface processes " Retrieved 19 December 2014, from http://www.pflotran.org/.

Lothenbach, B., T. Matschei, G. Möschner and F. P. Glasser (2008). Thermodynamic modelling of the effect of temperature on the hydration and porosity of Portland cement. *Cement and Concrete Research* **38:** 1–18.

Marty, N. C. M., Claret, F., Lassin, A., Tremosa, J., Blanc, P., Madé, B., Giffaut, E., Cochepin, B., Tournassat, C. (2015) A database of dissolution and precipitation rates for clay-rocks minerals. *Applied Geochemistry* **55:** 108–118.

Mason, H. E., Wyatt L. Du Frane, W. L., Walsh, S. D. C., Dai, Z., Charnvanichborikarn, S., Carroll, S. A. (2013) Chemical and mechanical properties of wellbore cement altered by CO_2 rich brine using a multianalytical approach. *Environmental Science & Technology* **47:** 1745−1752.

Matschei, T., B. Lothenbach and F. Glasser (2007). Thermodynamic properties of Portland cement hydrates in the system CaO-Al_2O_3-SiO_2-$CaSO_4$-$CaCO_3$-H_2O. *Cement and Concrete Research* **37(10):** 1379–1410.

Mito, S., Xue, Z., Sato, H. (2015) Experimental assessment of well integrity for CO_2 geological storage: Batch experimental results on geochemical interactions between a CO_2-brine mixture and a sandstone–cement–steel sample. *International Journal of Greenhouse Gas Control* **39:** 420–431.

Newell, D. L., Carey, J. W. (2012) Experimental evaluation of wellbore integrity along the cement rock boundary. *Environmental Science & Technology* **47:**276–282.

Pawar, R.; Bromhal, G.; Carroll, S.; Chu, S.; Dilmore, R.; Gastleum, J.; Oldenburg, C.; Stauffer, P.; Zhang, Y.; Guthrie, G. (2014) Quantification of Key Long-term Risks at CO_2 Sequestration Sites: Latest Results from US DOE's National Risk Assessment Partnership (NRAP) Project. *Energy Procedia* **63*:***4816–4823.

Pawar, R.; Bromhal, G.; Dilmore, R.; Oldenburg, C. M.; Zhang, Y.; Guthrie, G.; Chu, S. (2016) The National Risk Assessment Partnership's Integrated Assessment Model for Carbon Storage: A Tool to Support Decision Making Amidst Uncertainty. *International Journal of Greenhouse Gas Control* **52:**175-189.

Scherer, G. W., M. A. Celia, J.-H. Prevost, S. Bachu, R. Bruant, A. Duguid, R. Fuller, S. E. Gasda, M. Radonjic and W. Vichit-Vadakan (2005). Leakage of CO_2 through abandoned wells: Role of corrosion of cement. *Geologic Storage of Carbon Dioxide with Monitoring and Verification*. S. M. Benson. London, UK, Elseivier. **2:** 827–850.

Scherer, G. W., B. G. Kutchko, N. Thaulow, A. Duguid and B. Mook (2011). Characterization of cement from a well at Teapot Dome Oil Field: Implications for geological sequestration. *International Journal of Greenhouse Gas Control* **5:** 115–124.

Stauffer, P. H., Viswanathan, H. S., Pawar R. J., Guthrie, G. D. (2009) A System model for geologic sequestration of carbon dioxide. *Environmental Science and Technology*, **43:**565–570.

Tremosa, J., Mito, S., Audigane, P., Xue, Z. (2017) Experimental assessment of well integrity for CO_2 geological storage: A numerical study of the geochemical interactions between a CO_2-brine mixture and a sandstone-cement-steel sample. *Applied Geochemistry* **78:** 61–73.

Verba, C., W. O. O'Connor, G. Rush, J. Palandri, M. Reed and J. Ideker (2014). Geochemical alteration of simulated wellbores of CO_2 injection sites within the Illinois and Pasco basins. *International Journal of Greenhouse Gas Control* **23:** 119–134.

Viswanathan, H. S., Pawar R. J., Stauffer, P. H., Kaszuba, J. P. Carey, J. W., Olsen, S. C., Keating, G. N., Kavetski, D., Guthrie, G. D. (2008) Development of a hybrid process and system model for the assessment of wellbore leakage at a geologic CO_2 sequestration site. *Environmental Science and Technology*, **42:**7280–7286.

Walsh, S. D. C., H. E. Mason, W. L. Du Frane and S. A. Carroll (2014). Experimental calibration of a numerical model describing the alteration of cement/caprock interfaces by carbonated brine. *International Journal of Greenhouse Gas Control* **22:** 176–188.

Walsh, S. D. C., H. E. Mason, W. L. Du Frane and S. A. Carroll (2014). Mechanical and hydraulic coupling in cement–caprock interfaces exposed to carbonated brine. *International Journal of Greenhouse Gas Control* **25:** 109–120.

Wigand, M., Kaszuba, J.P., Carey, J.W., Hollis, W.K. (2009). Geochemical effects of CO_2 sequestration on fractured wellbore cement at the cement/caprock interface. *Chemical Geology* **265:**122–133.

Wolterbeek,T, K. T. , Peach, C. J., Raoof, A., Spiers, C. J. (2016) Reactive transport of CO_2-rich fluids in simulated wellbore interfaces:Flow-through experiments on the 1–6 m length scale. *International Journal of Greenhouse Gas Control* **54:** 96–116.

Zhang, L., D. Dzombak, D. Nakles, J. Brunet and L. Li (2013). Reactive Transport Modeling of Interactions between Acid Gas (CO_2 + H_2S) and Pozzolan-amended Wellbore Cement under Geologic Carbon Sequestration Conditions. *Energy and Fuels* **27:** 6921–6937.

Zhang, L., D. A. Dzombak, D. V. Nakles, S. B. Hawthorne, D. J. Miller, B. G. Kutchko, L. C. L. and B. R. Strazisar (2013). Characterization of pozzolan-amended wellbore cement exposed to CO_2 and H_2S gas mixtures under geologic carbon sequestration conditions. *International Journal of Greenhouse Gas Control* **19:** 358–368.

Zhang, M. and S. Bachu (2011). Review of integrity of existing wells in relation to CO_2 geological storage: What do we know? *International Journal of Greenhouse Gas Control* **5:** 826–840.

Zimmerman, R. W. and Bodvarsson, G. S. (1994) Hydraulic Conductivity of Rock Fractures. Lawrence Berkeley Laboratory LBL-35976 (/www.osti.gov/scitech/servlets/purl/60784).

Zyvoloski, G.A. (2007) FEHM: a control volume finite element code for simulating subsurface multi-phase multi-fluid heat and mass transfer. Los Alamos Unlimited Release report **LAUR-07-3359**. Los Alamos National Laboratory, Los Alamos, NM.

Appendix I: Additional Details on the Thermodynamic Model

Thermodynamic Model for CO_2 Solubility

The solubility of CO_2 was consistent with values reported by Duan and Sun (2003). Duan and Sun report values for total dissolved carbon dioxide as a function of temperature and pressure for pure water and sodium chloride brine solutions (1 molal, 2 molal, and 4 molal) based on an equation of state that they developed from a variety of experimental studies.

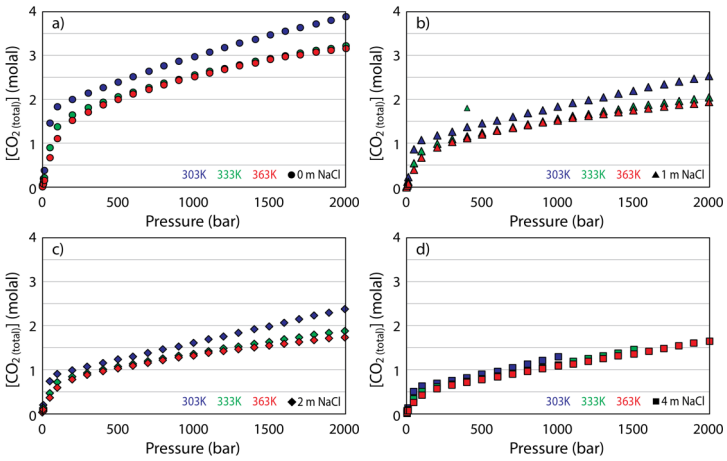

Figure A-I.1. Aqueous $CO_{2\ (total)}$ versus pressure as reported in Duan and Sun (2003) for concentrations of NaCl of 0 molal (a), 1 molal (b), 2 molal (c), and 4 molal (d) and for temperatures of 303.15K (blue), 333.15K (green), and 363.15K (red).

The original values reported by Duan and Sun are shown in Figure A-I.1. In general, dissolved CO_2 increases as a function of pressure and decreases as a function of both temperature and salinity (as NaCl). Note: the value reported in Duan and Sun (2003) for 400 bar and 333.15K (1.8127; shown as a small green triangle on Fig. A-I.1-b) appears to be a typographic error, and a transposition of numbers (1.8127 to 1.1827) brings the value in line with other values reported for 333.15K. This transposed value was used in calculation of the fugacities for this study.

We conducted a series of simulations in PFLOTRAN to calibrate our model to the model of Duan and Sun. A separate carbon-dioxide fluid was used as a buffering phase by setting its fugacity in conjunction with the equilibrium constant give in Table 1. An initial set of calculations at a fugacity of 100 bars was used to calibrate the fugacity setting the summation of calculated molalities for HCO_3^-, CO_3^{2-}, $CO_{2\ (aq)}$, $CaCO_{3\ (aq)}$, $CaHCO_3^{+}{}_{(aq)}$, $NaCO_3^-$, and $NaHCO_{3\ (aq)}$ to the value of $CO_{2\ (total)}$ as given in Duan and Sun (2003). These were then used to develop calibration curves for fugacity as a function of pressure, temperature, and concentration of NaCl as shown in Table A-I.1.

Table A-I.1. Fugacity for CO_2(g) calibrated to produce total aqueous CO_2 values as reported by Duan and Sun (2003) when used with an equilibrium constant for CO_2 (g) $\rightarrow HCO_3^-$ as given in Table 1.

P (bars)	Fugacity (bars) 0 molal NaCl			Fugacity (bars) 1 molal NaCl			Fugacity (bars) 2 molal NaCl			Fugacity (bars) 4 molal NaCl		
	303 K	333 K	363 K									
1	0.94	0.85	0.31	0.79	0.72	0.27	0.66	0.62	0.24	0.48	0.48	0.18
5	4.76	4.97	4.47	3.91	4.17	3.78	3.25	3.54	3.25	2.32	2.65	2.51
10	9.27	9.91	9.50	7.57	8.26	7.99	6.25	6.96	6.82	4.42	5.15	5.18
50	35.67	41.43	43.30	28.79	34.03	35.86	23.53	28.35	30.16	16.31	20.50	22.32
100	44.90	63.58	71.86	36.14	51.99	59.15	29.48	43.16	49.50	20.41	31.10	36.44
200	49.12	76.38	98.87	39.55	62.30	80.93	32.33	51.70	67.55	22.59	37.48	49.86
300	52.75	83.50	111.93	42.58	68.12	91.39	34.96	56.66	76.31	24.78	41.54	56.84
400	56.10	89.58	122.00	45.45	73.16	99.49	37.52	61.07	83.19	27.04	45.40	62.66
500	59.27	95.09	130.75	48.22	77.80	106.56	40.05	65.21	89.29	29.37	49.20	68.11
600	62.30	100.20	138.64	50.92	82.16	112.97	42.56	69.17	94.91	31.79	53.01	73.37
700	65.21	105.00	145.91	53.56	86.30	118.91	45.07	73.00	100.19	34.29	56.86	78.54
800	68.03	109.54	152.69	56.16	90.27	124.47	47.58	76.73	105.19	36.90	60.77	83.67
900	70.76	113.84	159.03	58.71	94.08	129.70	50.09	80.37	109.97	39.60	64.74	88.77
1000	73.42	117.95	164.98	61.23	97.75	134.63	52.61	83.94	114.53	42.42	68.78	93.86
1100	75.99	121.84	170.58	63.72	101.29	139.30	55.13	87.44	118.92	—	72.90	98.94
1200	78.49	125.56	175.84	66.17	104.70	143.71	57.67	90.86	123.12	—	77.09	104.02
1300	80.92	129.10	180.79	68.59	107.99	147.88	60.21	94.23	127.15	—	81.36	109.12
1400	83.27	132.45	185.44	70.97	111.16	151.82	62.76	97.52	131.03	—	85.71	114.21
1500	85.55	135.65	189.79	73.33	114.21	155.53	65.32	100.75	134.72	—	90.14	119.31
1600	87.77	138.68	193.85	75.65	117.15	159.03	67.89	103.92	138.28	—	—	124.41
1700	89.90	141.54	197.64	77.92	119.96	162.29	70.45	107.01	141.66	—	—	129.50
1800	91.98	144.24	201.15	80.18	122.66	165.36	73.03	110.04	144.90	—	—	134.59
1900	93.98	146.80	204.41	82.38	125.25	168.23	75.61	113.01	147.98	—	—	139.69
2000	95.91	149.18	207.38	84.55	127.72	170.87	78.19	115.88	150.89	—	—	144.76

Figures A-I.2–A-I.4 show the behavior of the calibrated fugacity as a function of pressure, temperature, and salinity. Variation as a function of pressure has a slight curvature, especially at lower pressures; however, in general a linear interpolation would reproduce intermediate values that are close to the projected Duan and Sun values. Variation in fugacity as a function of salinity (Fig. A-I.3) or of temperature (Fig. A-I.4) are very close to linear, justifying a linear interpolation for intermediate values.

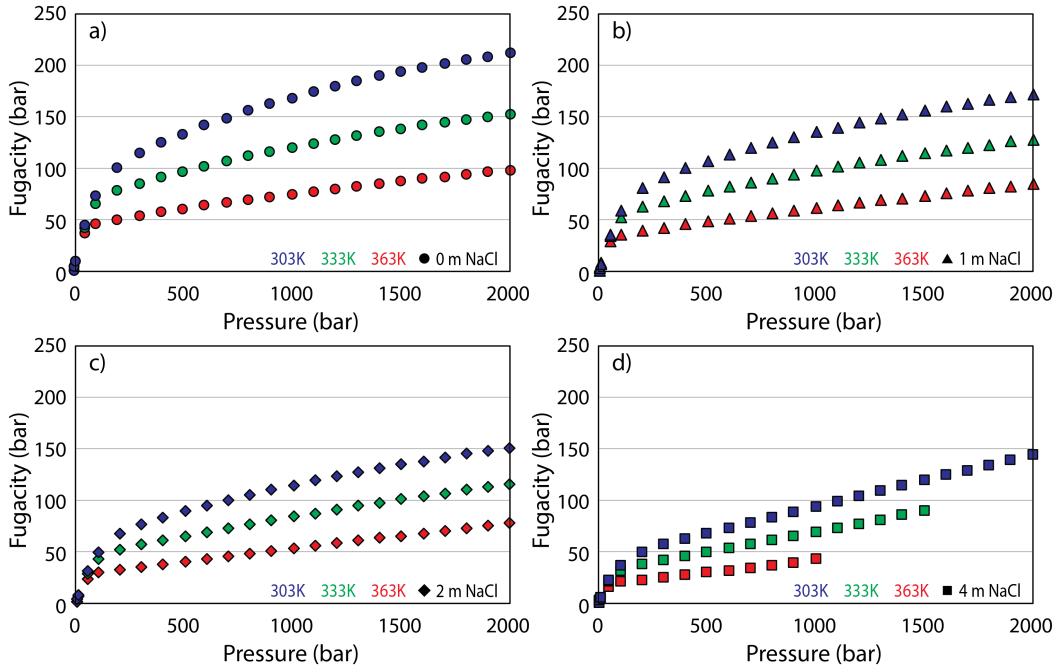

Figure A-I.2. Variation in calibrated fugacity as a function of pressure for concentrations of NaCl of 0 molal (a), 1 molal (b), 2 molal (c), and 4 molal (d) and for temperatures of 303.15K (blue), 333.15K (green), and 363.15K (red).

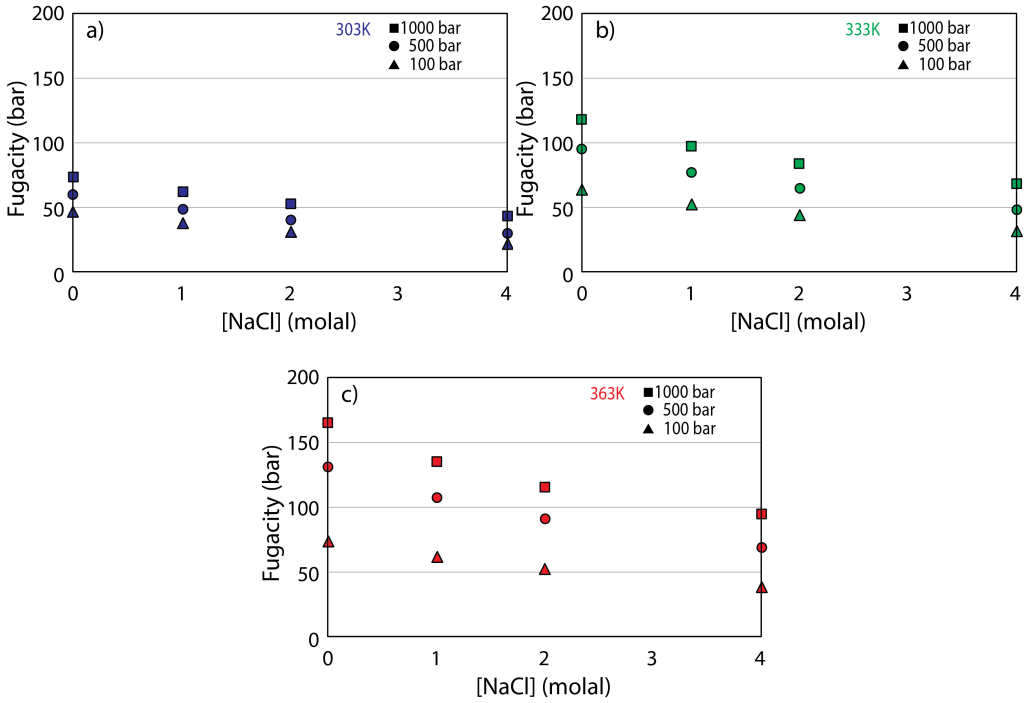

Figure A-I.3. Variation in calibrated fugacity as a function of concentration of sodium chloride for temperatures of 303.15K (a), 333.15K (b), and 363.15K (c) and for pressures of 100 bar (triangles), 500 bar (circles), and 1000 bar (squares).

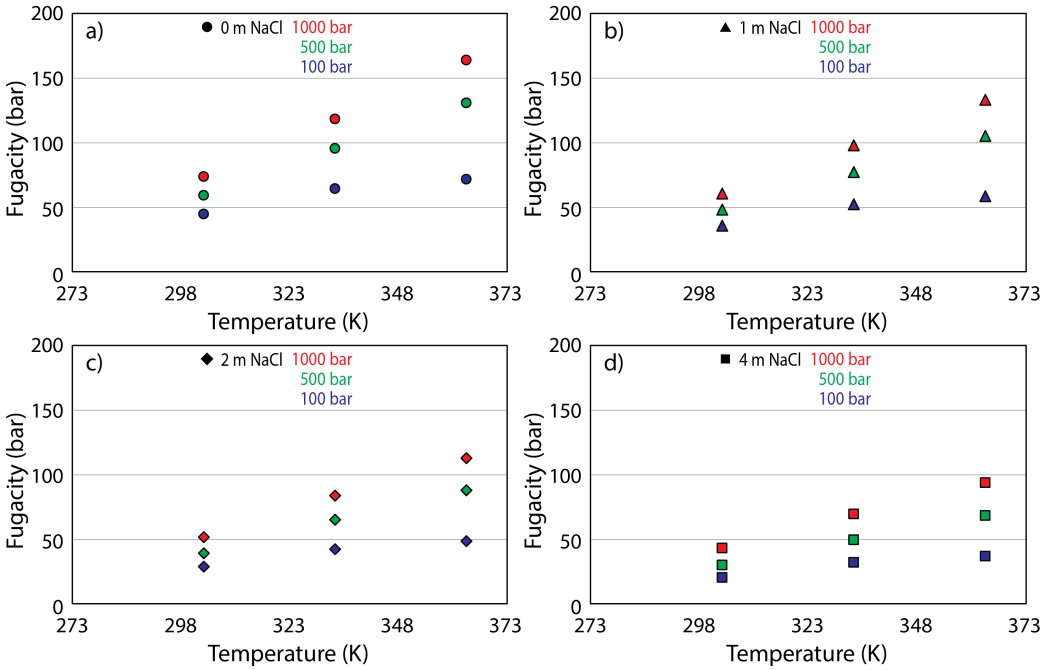

Figure A-I.4. Variation in calibrated fugacity as a function of temperatures for sodium-chloride concentrations of 0 molal (a), 2 molal (b), 3 molal (c), and 4 molal (d) and for pressures of 100 bar (blue), 500 bar (green), and 1000 bar (red).

Figure A-I.5 shows the pH behavior of the Duan-Sun model as implemented in PFLOTRAN, using pH as an indicator. This parameter is shown because pH is important in both the chemical equilibria and the reaction rates, and this is particularly true of the mineralogical system represented in wellbore integrity (where the reactions are driven largely by the pH gradient between cement and carbonated brine). As can be seen, the Duan and Sun model predicts values in the range of ~3.25>pH>3.0 for water saturated under most geologic storage conditions.

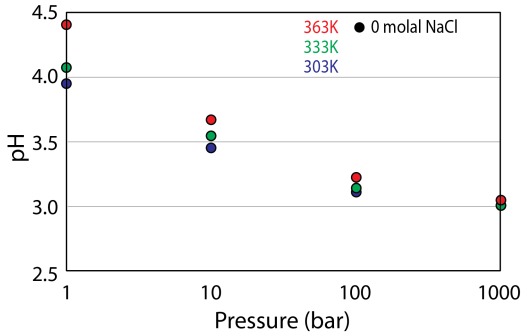

Figure A-I.5. Variation in calculated pH as a function of pressure for 0 molal NaCl at temperatures of 303.15K (blue), 333.15K (green), and 363.15K (red). Calculations were based on the calibrated "fugacity" values determined such that aqueous $CO_{2\ (total)}$ calculated by PFLOTRAN matched values reported by Duan and Sun (2003).

Thermodynamic Model for C–S–H

Several thermodynamic models have been reported for C–S–H, but most of these are applicable only at 25 °C. Two efforts have developed thermodynamic models that are applicable at elevated temperatures. The work of (Blanc, Lassin et al. 2012) provides a C–S–H model for three different Ca:Si ratios (0.8, 1.2, 1.6), and the work of Kulik and Kersten (2001) presents models for endmember compositions consistent with a jennite-like C–S–H (Ca:Si=1.67) and a tobermorite-like C–S–H (Ca:Si=0.83). Subsequent work by (Matschei, Lothenbach et al. 2007, Lothenbach, Matschei et al. 2008) also provides a model for C–S–H at elevated temperatures, but it is based on the model of Kulik and Kersten (2001).

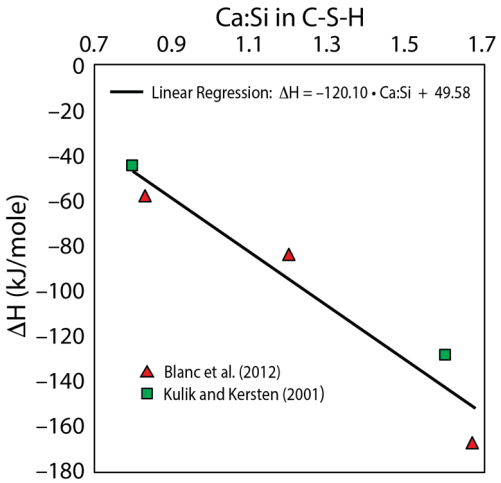

Figure A-I.6. Plot of $\Delta H_{reaction}$ for C–S–H as a function of the ratio of calcium to silicon. The solid line shows a linear regression of the data from Blanc et al. (2012) and Kulik and Kersten (2001), which was used in this study to extend the C–S–H model of Carey and Lichtner (2007) from 25 °C to higher temperatures.

Carey and Lichtner (2007) also present a thermodynamic model that treats C–S–H as a solid solution, allowing for a wider range of Ca:Si compositions to be explored. However, their model is limited to 25 °C. In the present study, we have extended that model to higher

temperatures using a $\Delta H_{reaction}$ derived from the models of Blanc et al. (2012) and Kulik and Kersten (2001). As shown in Figure A-I.6, the reported values for ΔH vary with the Ca:Si ratio in C–S–H. We assumed a linear fit to the reported values to derive ΔH values that could be used across the solid solution in the Carey and Lichtner model. That relationship is shown on Fig. A-I.6 and was used in conjunction with the Van 't Hoff equation to derive the logKs provided in Table 2.

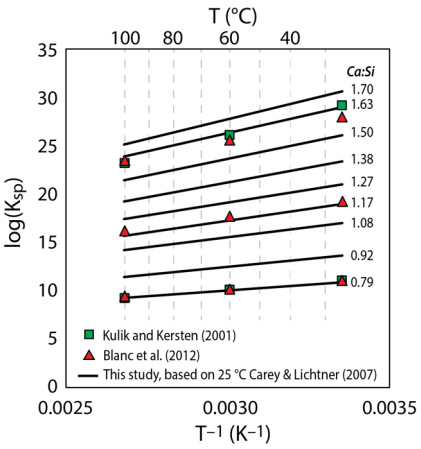

Figure A-I.7. Variation in logKs for C–S–H as a function of temperature. Ca:Si labels indicate lines for different C–S–H from the Carey and Lichtner model.

Figure A-I.7 shows the variation in logKs for the C–S–H models as a function of temperature. As can be seen, there is only a slight variation in the models with respect to slope (i.e., ΔH) and, in some cases, magnitude (e.g., the Kulik and Kersten values for Ca:Si=1.67 plot close to the Carey and Lichtner values for Ca:Si=1.63).

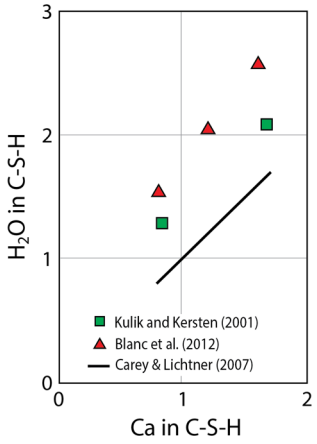

Figure A-I.8. Plot of the molar ratios water to calcium in C–S–H.

The two primary differences in the C–S–H models, however, are the assumptions on the amount of structural water and the molar-volume relationships. Figure A-I.8 shows a plot of H_2O vs. Ca for the three models. The Carey and Lichtner model assumes the lowest amount of structural water in C–S–H, and the Kulik and Kersten model assumes the highest amount. In the case of Carey and Lichtner, the Ca:H_2O ratio is 1:1, which reflects their assumption that C–S–H can be represented as a solid solution between $Ca(OH)_2$ and SiO_2. The exact structure and composition of C–S–H remain somewhat elusive due to the poorly crystalline and variable nature of the material, so the three models will be considered in our analysis (since they are each consistent with experimental data). Molar volume trends also differ for the three models (Fig. A-I.9). This difference has a significant impact on the predictions of volume increases, the net effect being that the Carey and Lichtner model is the most conservative relative to self sealing (albeit all three models are similar in their predictions of the pH transition).

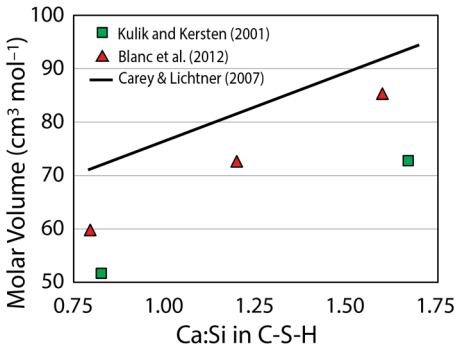

Figure A-I.9. Plot of molar volume for the various C–S–H models.

Simulation of Coupled Reservoir–Wellbore Flow

Simulation of wellbore leakage was based on a detailed physics-based model developed under the NRAP initiative (Harp et al., 2014; Jordan et al., 2015): It is a 3D continuum-scale Darcy's law model that includes reservoir, wellbore, and an overlying unit (e.g., thief zone or aquifer) implemented in LANL's FEHM simulator, which calculates heat and mass transfer based on multiphase, non-isothermal fluid flow using the controlled-volume, finite-element method (Zyvoloski, 2007; fehm.lanl.gov). The mesh is octree-refined in the lateral direction around the leaking wellbore to a 10 cm square wellbore using the meshing tool LaGriT (lagrit.lanl.gov). Caprock layers are removed to reduce computational and memory burden, expect for 8 m around the wellbore to model thermal effects on the surrounding caprock during CO_2 phase changes during leakage along the wellbore.

Our wellbore-leakage simulations focused only on non-reactive flow; we did not incorporate any mineralogical reactions or CO_2 dissolution into the aqueous phase. The goal of the simulations was simply to predict fluid velocities for different scenarios of reservoir permeability and ΔP.

The permeabilities of reservoir, wellbore, and thief zone were assumed to be homogenous. Permeability for the wellbore and thief zone was set to 10^{-10} m^2 (i.e., 100 d), whereas the reservoir permeability was varied over 0.01–1 d. Some runs were also conducted with a wellbore permeability of 10^{-11} m^2 (i.e., 10 d).

The pressure in the reservoir was calculated assuming a 1 Mt/yr injection of CO_2, starting with a reservoir pressure at hydrostatic conditions and a geothermal gradient of 0.03 ^{o}C/m.

The position of the leaking wellbore was 1 km from the injection well. The depth to the top of reservoir was 1 km. A thief zone was located at 300-m deep with a low permeability of 10^{-18} m^2.